Journal of Ultrafine Grained and Nanostructured Materials
https://jufgnsm.ut.ac.ir
Vol. 59, No.1, June 2026, pp. 126-149
Print ISSN: 2423-6845 Online ISSN: 2423-6837
DOI: 10.22059/jufgnsm.2026.01.10

Electrochemical Synthesis of Metal- and Nonmetal-Doped TiO_2 Nanotubes for Enhanced Photoelectrochemical Charge Transfer

Mohammed Ahmed Hussein Awad[1]*, Yasmin M.S. Jamil[2], Hussein M.A. Al-Maydama[2]

[1] Chemistry Department, Faculty of Applied Sciences, Thamar University, Thamar, Yemen.
[2] Department of Chemistry, Faculty of Science, Sana'a University, Yemen.

Recieved: 10 May 2026; Accepted: 21 June 2026

**Corresponding author, E-mail:* mohammed.awad@tu.edu.ye

ABSTRACT

In this work, self-ordered titanium dioxide (TiO_2) nanotubes (NTs) doped with various metal and nonmetal species were synthesized by in-situ electro-anodization to improve the photoelectrochemical (PEC) performance of TiO_2 nanotube arrays. The formation mechanism of the nanotubes was investigated through current density–time (J–t) behavior, which confirmed the successful development of nanotubular structures under all doping conditions. X-ray diffraction (XRD) analysis showed that the as-anodized TiO_2 NTs were amorphous, whereas annealing at 450 °C induced crystallization into the anatase phase. Doped samples, including 0.05 M V-doped TiO_2 NTs–N_2, 0.01 M W-doped TiO_2 NTs–N_2, and 0.05 M Fe-doped TiO_2 NTs–N_2, retained the anatase structure after doping and annealing, and no secondary dopant-related oxide phases were detected by XRD, although the presence of phases below the detection limit or in an amorphous state cannot be excluded. Minor peak broadening was attributed to lattice distortion and defect generation associated with dopant incorporation, which may contribute to improved charge separation and electronic conductivity in TiO_2-based photoelectrodes. Scanning electron microscopy (SEM) further confirmed the formation of vertically aligned and highly ordered nanotube arrays with uniform diameters ranging from 12 to 78 nm. The photoelectrochemical performance of the doped TiO_2 NTs was evaluated under ultraviolet (UV) illumination using linear sweep voltammetry (LSV) and chronoamperometry in three different electrolytes, namely 1 M KOH, 0.5 M H_2SO_4, and 0.5 M Na_2SO_4. Most doped samples exhibited higher photocurrent densities than the undoped TiO_2 NTs, particularly in alkaline media, and KOH produced the highest and most stable photocurrent response among the investigated electrolytes. These findings indicate that both the dopant type and electrolyte environment significantly influence the photoelectrochemical behavior of TiO_2 nanotubes. The improved performance is reflected by enhanced photocurrent generation and operational stability, suggesting more favorable interfacial charge-transfer processes and charge transport at the TiO_2/electrolyte interface under UV illumination.

Keywords: *Electrochemical anodization, TiO_2 nanotubes, In-situ metal and nonmetal doping, Photoelectrochemical performance, photocatalysts, Electrolyte effects.*

1. Introduction

Applications of metal nanoparticles loaded on metal oxide semiconductor surfaces are diverse and include environmental decontamination, wastewater treatment, pharmaceutical synthesis, photocatalytic fuel production, and other industrial photocatalysis processes [1]. Among these materials, TiO_2 is widely employed due to its stability, low cost, and favorable electronic properties. However, one of the main limitations of TiO_2 is the rapid recombination of photogenerated electron–hole pairs on its surface, which reduces photocatalytic efficiency [2]. To address this limitation and to meet the increasing global demand for clean and sustainable energy, hydrogen production via photoelectrochemical (PEC) water splitting has

emerged as a promising approach powered by solar energy [3–7]. The photoelectrochemical performance of TiO_2 can be significantly improved through surface and electronic modifications, including doping with non-metals or incorporating noble metal nanoparticles, which enhance charge separation and interfacial charge transfer under illumination [3–7]. Recent studies have shown that fluorine-modified TiO_2 exhibits improved hydrogen evolution activity [3], while Pt- or graphene-based composites further enhance charge transport and catalytic activity [4–6]. Moreover, ion-modified TiO_2 systems also demonstrate improved photoelectrochemical behavior due to tunable electronic properties [7].

An inexpensive, non-toxic, chemically and thermally stable, and environmentally benign n-type semiconductor photocatalyst, TiO_2 exhibits minimal photocorrosion characteristics. Its favorable band-edge positions and long electron lifetime in the anatase phase make it a widely studied material for environmental remediation and solar-to-chemical energy conversion. However, the large band gap of TiO_2 restricts its optical absorption to the ultraviolet (UV) portion of the solar spectrum, which constitutes only a small fraction (3–4%) of solar radiation. Therefore, efficient photoelectrochemical operation of TiO_2 is mainly achieved under UV illumination, which provides sufficient photon energy to generate electron–hole pairs.

To enhance UV-driven photoelectrochemical performance, extensive strategies have been developed to improve charge separation and suppress recombination. These include doping with non-metals [8,9], noble metals [10,11], transition metals [12,13], carbon-based materials [14], enzymes [15], and lanthanide elements [16–19]. Although other semiconductor systems such as ZnO, WO_3, and ZrO_2 have been investigated, TiO_2 remains the most widely used material due to its stability, favorable band alignment, and long carrier lifetime [20]. However, fast electron–hole recombination and UV-dependent activation remain key limitations [21,22].

To overcome these limitations under UV operation, several strategies have been developed, including noble-metal deposition, dye sensitization, heterojunction formation, and elemental doping [21]. Transition metal doping such as chromium introduces defect states that act as charge trapping centers, improving electron–hole separation and enhancing photoelectrochemical activity under UV irradiation [23]. These dopants also reduce recombination probability and extend carrier lifetime [23–25].

By modifying electronic structure via d-orbital states or introducing trap states, transition metals can significantly enhance UV-driven photoelectrochemical activity of TiO_2 nanotubes (NTs) [26–28]. In addition, surface modification with co-catalysts improves interfacial charge transfer [29]. For example, copper or copper oxide deposition on anodic TiO_2 NTs has been widely reported to enhance photoelectrochemical performance under UV illumination [30].

Modern morphological engineering combined with doping strategies has been shown to improve TiO_2 UV activity. One-dimensional nanotube architectures together with non-metal doping such as nitrogen significantly enhance charge separation and photocatalytic performance under UV conditions [31]. More recent studies demonstrate that doping TiO_2 with carbon [32], fluorine [33], iodine [34], and nitrogen [35] improves UV-driven photoelectrochemical activity by introducing oxygen vacancies or modifying defect states [36]. In addition, N–F co-doping exhibits synergistic effects that further enhance UV photoelectrochemical performance [37]. Despite these advances, reports on multi-non-metal doping remain limited, indicating the need for further investigation.

TiO_2 remains one of the most efficient UV-active photocatalysts, but its performance is strongly influenced by morphology and surface area. One-dimensional nanotube structures significantly enhance charge transport and reduce recombination. Electrochemical anodization enables fabrication of highly ordered TiO_2 nanotube (NT) arrays with diameters ≈100 nm and lengths exceeding 500 nm [38–40]. The formation and geometry of nanotubes can be tuned through electrolyte composition, including NH_4F-containing solutions [41,44], NaF-based electrolytes [42,45], and glycerol/NH_4F mixtures [43,46]. Recent studies show that controlling anodization parameters such as voltage, temperature, and pH leads to improved nanotube ordering and enhanced photoelectrochemical performance [47].

This structural and compositional control provides a strong platform for improving UV-driven photoelectrochemical activity. In this work, we demonstrate a single-step in-situ anodization strategy for fabricating multi-non-metal-doped TiO_2 nanotubes, enabling simultaneous control of nanotube growth and dopant incorporation without post-synthetic treatment.

The electrolyte used consists of iodic acid (HIO_3) and oxalic acid ($C_2H_2O_4{\cdot}2H_2O$), with a trace amount of NH_4F. Oxalic acid promotes ordered nanotube formation and stabilizes oxide growth during anodization [48]. NH_4F provides fluoride species and may contribute nitrogen-related species during anodization [49], while HIO_3 introduces iodine species that modify defect chemistry and enhance UV photoresponse [36].

Non-metal doping strategies have been widely investigated to enhance UV photocatalytic activity of TiO_2. Landmark studies by Asahi et al. and Khan et al. demonstrated that nitrogen doping introduces localized states near the valence band, improving UV photoactivity [50,51]. Furthermore, nitrogen/fluorine (N/F) co-doped TiO_2 systems exhibit improved charge separation and enhanced UV-driven photocatalytic performance [52]. Despite extensive progress in post-synthesis doping, in-situ multi-element incorporation during anodization remains underexplored, particularly for UV-based photoelectrochemical systems.

The objective of this work is to develop a unified strategy for the fabrication of highly ordered self-organized TiO_2 nanotube arrays doped with metal and non-metal ions via a single-step anodization process, enabling uniform dopant incorporation while preserving nanotube integrity and eliminating additional post-synthetic modification steps. The formation mechanism of doped nanotubes is investigated through current density–time transient analysis to elucidate growth behavior, while structural evolution is examined using X-ray diffraction to assess lattice distortion, defect formation, and crystallite size variation induced by nitrogen annealing without the appearance of secondary phases, and scanning electron microscopy confirms the retention of highly ordered nanotubular morphology across all samples. The photoelectrochemical performance of metal- and non-metal-doped TiO_2 nanotubes is systematically evaluated under UV illumination to investigate the influence of dopant type and electrolyte composition on charge separation and recombination behavior using linear sweep voltammetry (LSV) and chronoamperometry (CA) in KOH, H_2SO_4, and Na_2SO_4 electrolytes.

This study provides insights into dopant engineering and electrolyte-controlled synthesis for improving the UV-driven photoelectrochemical activity and stability of TiO_2-based photoelectrodes, offering a scalable and controlled fabrication approach for TiO_2 nanotube arrays. A systematic comparative investigation of metal- and nonmetal-doped TiO_2 nanotubes prepared via single-step anodization under identical experimental conditions is presented, correlating dopant incorporation with structural evolution and photoelectrochemical performance. Overall, the results highlight the role of controlled single-step doping in tailoring the structural and electrochemical properties of TiO_2 nanotubes and provide a systematic framework for understanding their UV-driven photoelectrochemical behavior.

2. Experimental

2.1. Materials

The specifications of the materials used in this study are listed in Table 1. All aqueous solutions were prepared by deionized water generated using Milli-Q (resistance 18.2 MΩ cm, Millipore, Inc.).

2.2. Anodization process

Titanium dioxide nanotube (TiO_2 NT) arrays were fabricated via electrochemical anodic oxidation of titanium foils, following previously reported procedures [43,47,53–55]. Titanium sheets (2 × 2.5 cm, thickness 0.25 mm) were used as substrates. Prior to anodization, Ti foils were ultrasonically cleaned in deionized water, isopropanol, and acetone sequentially, and then air-dried. The anodization process was performed in a two-electrode system, using Ti foil as the anode and a platinum plate as the cathode, with an electrode spacing of 10 mm. Anodization was carried out at room temperature using a DC power supply (Agilent E3612A) coupled with a 5.5-digit multimeter. TiO_2 nanotubes were formed in 0.5 wt% HF electrolyte under an applied voltage of 20 V for 20 min. After anodization, the samples were rinsed thoroughly with deionized water. To induce crystallization, the as-prepared TiO_2 NTs were annealed at 450 °C in a nitrogen atmosphere for 3 h with a heating/cooling rate of 5 °C min^{-1}, yielding TiO_2 NTs/N_2. As demonstrated previously by Schmuki et al. [42,45], this anodic oxidation route enables the formation of highly ordered TiO_2 nanotube arrays.

2.3. In Situ Doping During Anodization

2.3.1. Metal-ion doping

Metal-doped TiO_2 NTs were prepared by adding metal precursors directly into the anodization electrolyte (0.5 wt% HF). The anodization was performed at 20 V using the same two-electrode configuration described above. The following dopant concentrations were used: 20 and 50 mM V, 10 and 50 mM W, and 50 mM for Mo, Cr, Fe, and Cu salts [23,25,56–59].

2.3.2. Multi-nonmetal doping (N, F, I)

Multi-nonmetal-doped TiO_2 NTs were synthesized via anodization in a mixed electrolyte consisting of 83.3 mM oxalic acid ($C_2H_2O_4{\cdot}2H_2O$), 1.0 wt% iodic acid (HIO_3), and 0.5 wt% NH_4F. Anodization was performed at 20 V under continuous magnetic stirring at room temperature.

After anodization, the samples exhibited a yellowish surface and were rinsed with deionized water and air-dried. All doped samples were subsequently annealed at 450 °C in N_2 atmosphere for 3 h (heating/cooling rate: 5 °C min^{-1}) to induce crystallization into the anatase phase.

Table 1- Chemicals and materials used

No.	Chemical Material	Formula	Purity/Grade	Supplier
1	Titanium foils (thickness 0.25 mm)	Ti	> 99.5%	Alfa Aesar (USA)
2	Isopropanol	$CH_3CHOHCH_3$	99.0%	WINLAB (UK)
3	Acetone	CH_3COCH_3	99.0%	Sigma-Aldrich (USA)
4	Hydrofluoric	HF	39–43%	Qualikems Fine Chemicals Pvt. Ltd, India
5	Potassium hydroxide (flakes)	KOH	Extra Pure	LOBA Chemie, India
6	Sulphuric acid	H_2SO_4	Analytical grade (AG)	Sigma-Aldrich (USA)
7	Sodium sulphate	Na_2SO_4	Analytical grade (AG)	Alfa Aesar (USA)
8	Sodium tungstate dihydrate	$Na_2WO_4{\cdot}2H_2O$	99.0%	Merck (Germany)
9	Oxalic acid	$C_2H_2O_4{\cdot}2H_2O$	99.0%	WINLAB (UK)
10	Iodic acid	HIO_3	AG	BDH Chemicals (UK)
11	Ammonium fluoride	NH_4F	AnalaR grade	BDH Chemicals (UK)
12	Ammonium meta vanadate	NH_4VO_3	AG	BDH Chemicals (UK)
13	Chromium (III) nitrate Nona hydrate	$Cr(NO_3)_3{\cdot}9H_2O$	99.0%	Sigma-Aldrich (USA)
14	Ammonium molybdate tetrahydrate	$NH_4)_6Mo_7O_{24}.4H_2O$	AG	Sigma-Aldrich (USA
15	Iron (III) nitrate nona-hydrate.	$Fe\ (NO_3)_3{\cdot}9H_2O$	98.0-101.0%	Alfa Aesar (USA)
16	Copper (II) Chloride	$CuCl_2.n\ H_2O$	AG	Alfa Aesar (USA)
17	Deionized water	H_2O	18.2 MΩ cm	Milli-Q system (Millipore, USA)

2.4. Physicochemical Measurements

2.4.1. X-ray diffraction (XRD)

The crystal structure of the samples was analyzed using an RIGAKU MiniFlex 100 X-ray diffractometer operating at 40 kV and 15 mA with Cu Kα radiation. Data were collected over a 2θ range of 5–85° in wide-angle mode. A monochromator was used, and the scan rate was 2–5° min^{-1}. Cooling water flow was maintained at 3.7 L min^{-1}.

2.4.2. Scanning electron microscope (SEM)

Surface morphology was examined using a JEOL JSM-6380LA scanning electron microscope. Measurements were conducted at an accelerating voltage of 5.0 kV.

2.5. Photoelectrochemical Measurements

Photoelectrochemical experiments were carried out using a BioLogic SP-150 potentiostat coupled with a MAX-303 xenon lamp (Asahi Spectra, 100% intensity) as the light source. A three-electrode cell was employed, consisting of the prepared TiO_2 electrode as the working electrode, a platinum wire as the counter electrode, and a saturated calomel electrode (SCE) as the reference electrode. Measurements were performed in 1 M KOH, 0.5 M H_2SO_4, and 0.5 M Na_2SO_4 electrolytes. Linear sweep voltammetry (LSV) was conducted at a scan rate of 50 mV s^{-1}. Photocurrent response was recorded at a fixed potential of 1.0 V vs. SCE under chopped illumination (light on/off cycles of 70 s). Data analysis was performed using EC-Lab software (version 10.1x). The UV irradiance of the xenon lamp at 5 cm distance was estimated to be 20–30 mW cm^{-2} over the 200–400 nm range, based on manufacturer specifications.

However, in this study, all electrochemical measurements were consistently conducted and reported versus the saturated calomel electrode (SCE), which is a widely accepted reference in photoelectrochemical studies. To maintain consistency and comparability within our dataset, we have retained the SCE scale throughout the manuscript.

SCE to RHE Conversion and pH Dependency: Electrochemical potentials in this study were measured relative to the Standard Calomel Electrode (SCE). To interpret these results accurately, especially in acidic electrolytes like hydrofluoric acid (HF), the potentials need to be converted to the Reversible Hydrogen Electrode (RHE) scale. The conversion equation is [60]:

$$E_{RHE} = E_{SCE} + 0.241 + 0.0591 \times pH \quad (1)$$

Where: E_{RHE} is the potential vs. RHE, E_{SCE} is the potential vs. SCE, 0.241 V is the standard SCE-RHE offset at 25°C, and 0.0591 x pH is the pH-dependent term based on the Nernst equation.

For a 0.5% HF electrolyte with pH ≈ 1.88, the conversion from E_{SCE} = 0.15, gives:

E_{RHE} = 0.15 + 0.241 + (0.0591 x 1.88) = 0.502 V.

To calculate the pH from the measured E_{SCE} and E_{RHE}, the equation can be rearranged as:

$$pH = E_{RHE} - E_{SCE} - 0.241/0.0591 \quad (2)$$

For example, with E_{RHE} = 0.502 V and E_{SCE} = 0.15 V, the pH is:

pH = (0.502 - 0.15 - 0.241) / 0.0591 = 1.88.

The SCE-to-RHE conversion requires both the standard offset and a pH correction, which is particularly important in acidic solutions such as HF. Accurate conversion ensures reliable interpretation of electrochemical data.

3. Results and Discussion

3.1. Study of the formation mechanism of the TiO_2 nanotubes

Study of the formation mechanism of the TiO_2 nanotubes has been of interest for the researchers that among all the theories two important theories including oxygen bubble [61] and field-assisted are challenging [62–64]. Field-assisted theory about TiO_2 nanotubes growth is based on 3 significant processes [65]:

1. oxidation by field-assisted at the metal/oxide interface, given by Eq. (3):

$$Ti + 2H_2O \rightarrow TiO_2 + 4H^+ + 4e^- \quad (3)$$

2. dissolution by field-assisted at the oxide/electrolyte interface at the bottom of the nanotubes.
3. chemical etching at the top of the nanotubes.

Chemical interactions of these two last cases is given by Eq. (4):

$$TiO_2 + 6F^- + 4H^+ \rightarrow TiF_6^{2-} + 2H_2O \quad (4)$$

The collective effects of them will decide the final morphologies of the TiO_2 nanotubes. Figure 1 shows the current density–time curves obtained during anodization process. Regardless of the anodization time, all the curves show approximately same behavior. At the first stage, the sharp drop in the current density is due to the oxide layer formation on the Ti surface [66], which decreases the conduction resulting in sharp drop in the current density. At the second stage, current density is increased, indicating the pore formation. At the next stage, current density is decreased and remains constant. At this stage, oxide growth rate in the oxide/metal interface and oxide dissolution rate at the electrolyte/nanotube bottom are in equilibrium [66].

3.2. Physicochemical Characterization

3.2.1. XRD Analysis

XRD patterns of the as-anodized foils show the occurrence of the substrate Ti maxima only indicating that the TiO_2 nanotubes are X-ray amorphous. Calcination of the as-anodized TiO_2 foils, including the doped samples at 450 °C for 20 min leads to crystallization of TiO_2. All XRD patterns of the calcinated samples are similar and besides the intense Ti maxima exhibit also weak maxima of the anatase phase (Fig. 2). Figure 2 shows the XRD measurement result of TiO_2 NTs formed after annealing in nitrogen. The titania is a polycrystalline nature material; therefore, two peaks are observed after annealing in nitrogen. The diffraction of anatase TiO_2 A(004) and anatase TiO_2 (220) planes, related to the formation of TiO_2 NT, is observed on the peaks at 2θ = 38.4°, 40.2°, and 70.6° [67,68].

X-ray diffraction (XRD) analysis of TiO_2 nanotube arrays (TiO_2 NT arrays) fabricated via anodization in fluoride-containing electrolytes typically reveals an amorphous structure prior to annealing, because the field-assisted oxidation and simultaneous F^--etching suppress long-range crystallization during growth at room temperature [69]. Consequently, the as-anodized samples exhibit no anatase or rutile reflections, and only the diffraction peaks of the underlying Ti substrate appear. After thermal treatment in nitrogen, the amorphous nanotube walls convert into the anatase phase, as indicated by the emergence of sharp diffraction peaks at 2θ ≈ 25.4°, 38.4°, 52.97°, and 70.6° corresponding to the (101), (004), (105), and (220) planes of anatase TiO_2 [69,70]. The nanotubular architecture remains intact during

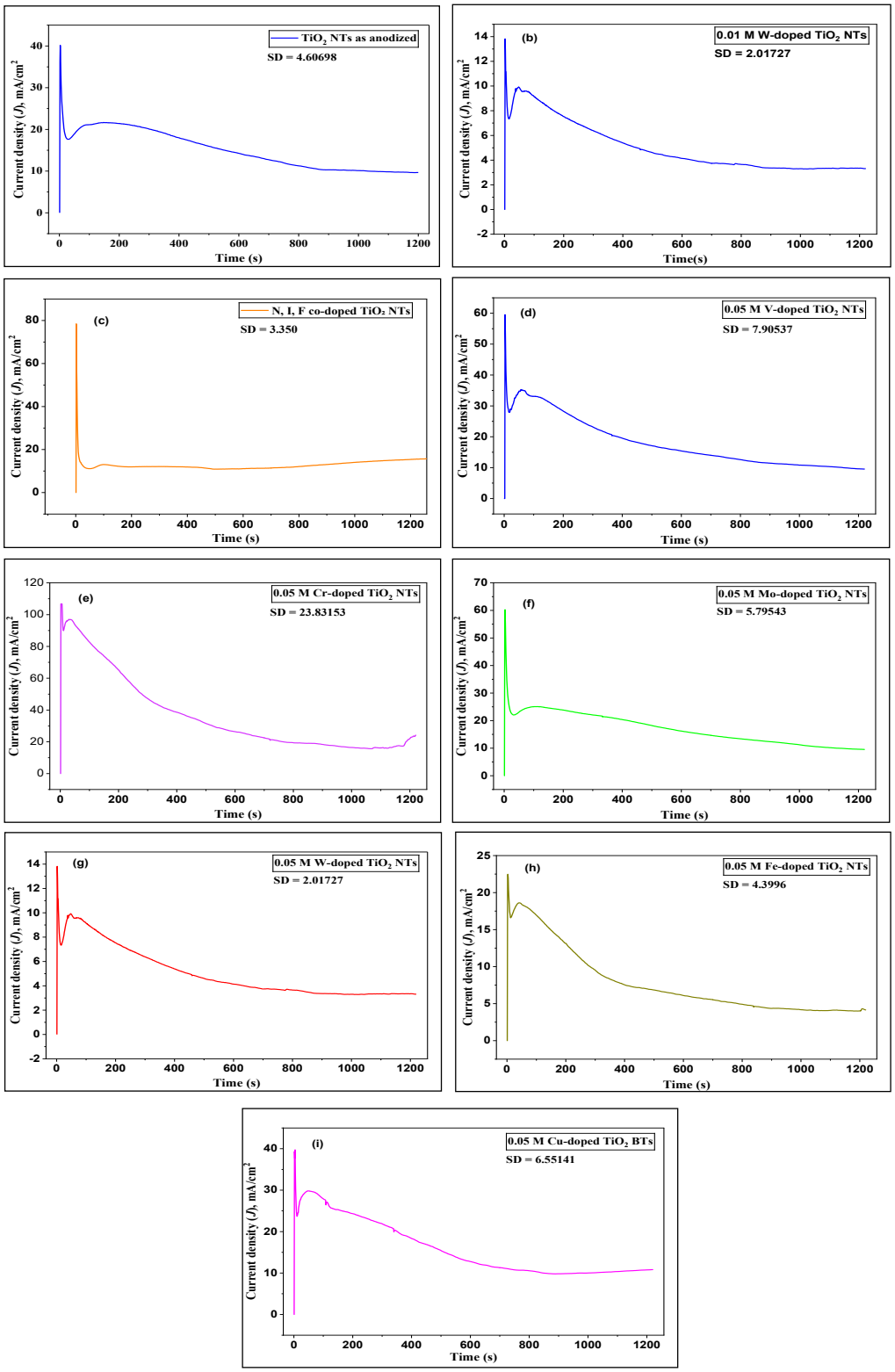

Fig. 1- Current density–time (J–t) profiles recorded during the anodization of TiO_2 nanotube arrays at a constant potential of 20 V for 20 min in an electrolyte containing 0.5 wt.% HF. (a) Undoped TiO_2 NTs; (b) in situ 0.01 M W-doped TiO_2 NTs; (c) in situ N, I, F co-doped TiO_2 NTs; (d) in situ 0.05 M V-doped TiO_2 NTs; (e) in situ 0.05 M Cr-doped TiO_2 NTs; (f) in situ 0.05 M Mo-doped TiO_2 NTs; (g) in situ 0.05 M W-doped TiO_2 NTs; (h) in situ 0.05 M Fe-doped TiO_2 NTs; (i) in situ 0.05 M Cu-doped TiO_2 NTs.

this amorphous-to-anatase transition, retaining the high-aspect-ratio morphology essential for catalytic and electrochemical applications [69]. When annealing is carried out in an N_2 atmosphere, nitrogen incorporation and oxygen-vacancy formation may occur, generating lattice distortion and defect states that can manifest in XRD as slight peak broadening or minor peak shifts without the appearance of new crystalline phases [71]. These structural modifications are consistent with recent studies demonstrating that N-doped TiO_2 retains its anatase framework while benefiting from enhanced optical and catalytic properties due to defect engineering [71,72].

X-ray diffraction (XRD) analysis of TiO_2 nanotube arrays doped with 0.05 M vanadium and annealed in air at 450 °C confirms the transformation of the as-anodized amorphous TiO_2 into the anatase phase, with diffraction peaks at $2\theta \approx 25.4°$, 38.4°, 52.97°, and 70.6° corresponding to the (101), (004), (105), and (220) planes, respectively. No additional peaks corresponding to V_2O_5 or other vanadium oxides are observed, indicating that vanadium ions are incorporated substitutionally into the TiO_2 lattice rather than forming separate oxide phases. The V-doping induces lattice distortions and oxygen vacancies, which are reflected as slight peak broadening and minor shifts in the XRD pattern, while the nanotubular morphology remains intact. Such structural modifications are consistent with enhanced electronic and photocatalytic properties reported for V-doped TiO_2 nanotubes and anatase nanostructures [73,74].

X-ray diffraction (XRD) of the W-doped TiO_2 nanotube arrays (prepared in situ in 0.5 wt.% HF and annealed in N_2 at 450 °C for 3 h) confirms that the nanotubes crystallize predominantly into the anatase TiO_2 phase, as indicated by the characteristic reflections at ~25.14° (101), 38.3° (004), 52.9° (105), and 70.5° (220). A slight shift of the anatase (101) peak toward lower 2θ values is observed, reflecting lattice expansion caused by substitution of Ti^{4+} with the larger W^{6+} cations. This effect is consistent with previous reports showing that tungsten incorporation distorts the anatase lattice and suppresses the anatase → rutile phase transition due to the strong interaction between W and Ti–O bonding networks [75,76]. Annealing in N_2 introduces oxygen vacancies (V_o) and partial reduction of Ti^{4+} to Ti^{3+}, which typically contributes to peak broadening and strain-related distortion within the lattice. At low tungsten concentrations, no crystalline WO_3 peaks appear in the XRD pattern, indicating that W is largely incorporated into the TiO_2 lattice rather than forming segregated oxide phases. This behavior agrees with literature, which also shows that W doping stabilizes the anatase structure and delays phase transformation even at elevated temperatures [77,78].

X-ray diffraction (XRD) analysis of the Fe-doped TiO_2 nanotubes prepared by in-situ anodization in 0.5 wt% HF and annealed at 450 °C in nitrogen confirms the formation of the anatase phase. The diffraction pattern shows the characteristic anatase reflections, with the dominant (101) peak at ~25.3°, along with the (004), (105), and (220) reflections at ~38.3°, 52.9°, and 70.52°, respectively [79]. No secondary iron-oxide phases (Fe_2O_3 or Fe_3O_4) are detected, indicating that Fe^{3+} ions are incorporated substitutionally into the TiO_2 lattice rather than forming separate crystalline Fe-oxidic domains [80]. Additionally, the anatase (101) peak exhibits noticeable broadening and a slight shift toward higher 2θ values compared to undoped

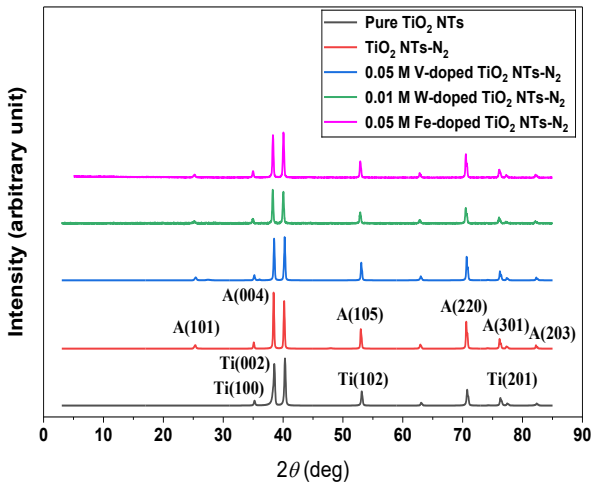

Fig. 2- X-ray diffraction (XRD) patterns of as-anodized pure TiO_2 NTs, TiO_2 NTs-N_2, 0.05 M V-doped TiO_2 NTs-N_2, 0.01 M W-doped TiO_2 NTs-N_2, and 0.05 M Fe-doped TiO_2 NTs-N_2.

TiO_2 nanotubes, which is consistent with lattice contraction caused by the smaller ionic radius of Fe^{3+} relative to Ti^{4+} and the generation of oxygen-vacancy defects under nitrogen annealing [81]. These findings confirm that nitrogen annealing converts the initially amorphous nanotube layer into Fe-doped anatase TiO_2 with enhanced defect density and without formation of detectable secondary phases.

The XRD patterns of TiO_2 NTs–N_2, 0.01 M W-doped TiO_2 NTs–N_2, and 0.05 M Fe-doped TiO_2 NTs–N_2 are presented in Figure 2. All samples exhibit the characteristic reflections of the anatase TiO_2 phase, with no secondary impurity peaks detected, confirming that W and Fe are successfully incorporated into the TiO_2 lattice without altering the crystalline phase. Compared to the undoped sample, both W- and Fe-doped samples show noticeable peak broadening, indicating the presence of lattice strain and reduced coherent domain sizes.

Crystallite sizes were calculated from the full width at half maximum (FWHM) of each diffraction peak using the Debye–Scherrer equation [82,83]:

$$D = \frac{K\lambda}{\beta_{hkl}\cos\theta} \quad (5)$$

where D is the average particle size, K is constant (0.9) (shape factor, dimensionless factor), λ is the wavelength of the x-ray (λ = 0.15406 nm), β_{hkl} is the full width at half-maximum of the peak (rad) (FWHM), and θ is the position of the diffraction peak.

The FWHM values were converted from degrees to radians (β = FWHM × π/180), and the corresponding Bragg angles were converted to θ in radians before applying the equation. The crystallite sizes calculated for each (hkl) reflection are summarized in Table 2, and the final average crystallite size ($D_{average}$) was obtained by averaging all individual values.

Table 2- Peak positions, FWHM values, and calculated crystallite sizes for TiO_2 NTs–N_2, 0.01 M W-doped TiO_2 NTs–N_2, and 0.05 M Fe-doped TiO_2 NTs–N_2. The average crystallite size (Daverage) was obtained by averaging the Scherrer -calculated sizes from all major reflections

Plane (*hkl*)	2θ (deg)	θ (deg)	θ (rad)	Cos (θ) rad	FWHM (deg)	β = [FWHM] (rad)	$D_{Scherrer}$ (nm)	$D_{average}$ (nm)
TiO_2 NTs-N_2 sample								
A(101)	25.376	12.688	0.221335111	0.975605219	0.307	0.005355444	26.55	
Ti(100)	35.087	17.544	0.221335111	0.953535153	0.196	0.003419111	42.54	
A(004)	38.408	19.204	0.335003111	0.944409287	0.159	0.002773667	52.95	
Ti(101)	40.175	20.088	0.350415278	0.939230234	0.184	0.003209778	46.00	
A(105)	52.971	26.486	0.462024833	0.89515174	0.159	0.002773667	55.86	48.67
A(204)	62.881	31.441	0.548462056	0.853327377	0.203	0.003541222	45.89	
A(220)	70.592	35.296	0.615719111	0.816358338	0.166	0.002895778	58.67	
A(301)	76.157	38.079	0.664258278	0.787374255	0.179	0.003122556	56.41	
Ti(201)	77.328	38.664	0.674472	0.781036788	0.28	0.004884444	36.36	
A(203)	82.209	41.105	0.717045167	0.753750816	0.161	0.002808556	65.51	
0.01 M W-doped TiO_2 NTs-N_2 sample								
A(101)	25.14	12.57	0.219276667	0.976055047	0.39	0.006803333	20.89	
Ti(100)	34.931	17.466	0.304675944	0.953944214	0.174	0.003035333	47.89	
A(004)	38.246	19.123	0.333590111	0.944872899	0.17	0.002965556	49.49	
Ti(101)	40.041	20.021	0.3492465	0.93963082	0.202	0.003523778	41.89	
A(105)	52.861	26.431	0.461065389	0.895579012	0.195	0.003401667	45.53	45.84
A(204)	62.798	31.399	0.547738111	0.853704601	0.18	0.00314	51.74	
A(220)	70.506	35.253	0.614969	0.816791332	0.192	0.003349333	50.69	
A(301)	76.055	38.028	0.663368611	0.787922401	0.206	0.003593556	48.98	
Ti(201)	77.16	38.58	0.673006667	0.781951028	0.2	0.003488889	50.84	
A(203)	82.13	41.065	0.716356111	0.754203457	0.209	0.003645889	50.44	
0.05 M Fe-doped TiO_2 NTs-N_2 sample								
A(101)	25.241	12.621	0.220157611	0.975863042	0.344	0.006000889	23.68	
Ti(100)	34.952	17.476	0.304859111	0.953889251	0.215	0.003750556	38.77	
A(004)	38.285	19.143	0.333930278	0.944761461	0.182	0.003174889	46.24	
Ti(101)	40.055	20.028	0.349368611	0.939589027	0.204	0.003558667	41.48	44.13
A(105)	52.882	26.441	0.461248556	0.895497505	0.177	0.003087667	50.16	
A(204)	62.805	31.403	0.547799167	0.853672804	0.186	0.003244667	50.07	
A(220)	70.516	35.258	0.615056222	0.816741008	0.174	0.003035333	55.94	
A(301)	76.091	38.046	0.663682611	0.787729009	0.214	0.003733111	47.16	
Ti(201)	77.26	38.63	0.673878889	0.78140704	0.234	0.004082	43.48	
A(203)	82.174	41.087	0.716739889	0.753951397	0.238	0.004151778	44.31	

The undoped TiO_2 NTs–N_2 exhibit the largest average crystallite size (48.67 nm), whereas W-doping reduces the size moderately (45.84 nm), and Fe-doping produces the smallest crystallites (44.13 nm). This reduction is attributed to the incorporation of W into the TiO_2 lattice, which induces local strain and restricts grain growth during annealing. Statistical analysis of the crystallite size distributions (standard deviation of individual (hkl) values) shows an increasing trend from TiO_2 NTs–N_2 ($\sigma \approx 7.89$ nm) to W-doped ($\sigma \approx 10.12$ nm) and Fe-doped ($\sigma \approx 11.27$ nm), reflecting the increasing structural heterogeneity with dopant incorporation.

This trend can be explained by ionic radius mismatch between the dopant and Ti^{4+}. Ti^{4+} has a radius of 0.605 Å, W^{6+} is very similar (~0.60 Å), and Fe^{3+} is larger (0.645 Å). Both smaller and larger dopants compared to Ti^{4+} introduce lattice strain, which inhibits crystal growth. In this study, the larger Fe^{3+} ion induces greater distortion than W^{6+}, restricting crystallite growth and resulting in the smallest particle sizes, whereas W^{6+} causes only minor strain, maintaining relatively larger crystallites. These observations are consistent with prior reports showing that transition-metal doping modulates TiO_2 crystallinity by introducing nanoscale lattice strain [81,82,83].

3.2.2. Size and Morphology

Figure 3A presents a top-view SEM image of the as-anodized TiO_2 nanotube (NT) array at 30,000× magnification, revealing a highly ordered and densely packed tubular architecture. The nanotubes exhibit a uniform and well-aligned structure with diameters ranging from 12 to 78 nm, consistent with previously reported self-organized TiO_2 nanotubes synthesized via electrochemical anodization [84–86]. This morphology originates from the dynamic balance between field-assisted oxide growth and chemical dissolution during the anodization process, which governs the formation of vertically aligned nanotubular arrays [84-87]. Such one-dimensional nanotubular structures provide a high surface-to-volume ratio and efficient charge transport pathways, which are highly beneficial for catalyst immobilization and electrochemical applications [85,88]. The particle size distribution analysis (Figure 3B) further confirms a narrow distribution with an average diameter of 48.75 nm, indicating good structural uniformity of the synthesized TiO_2 nanotubes.

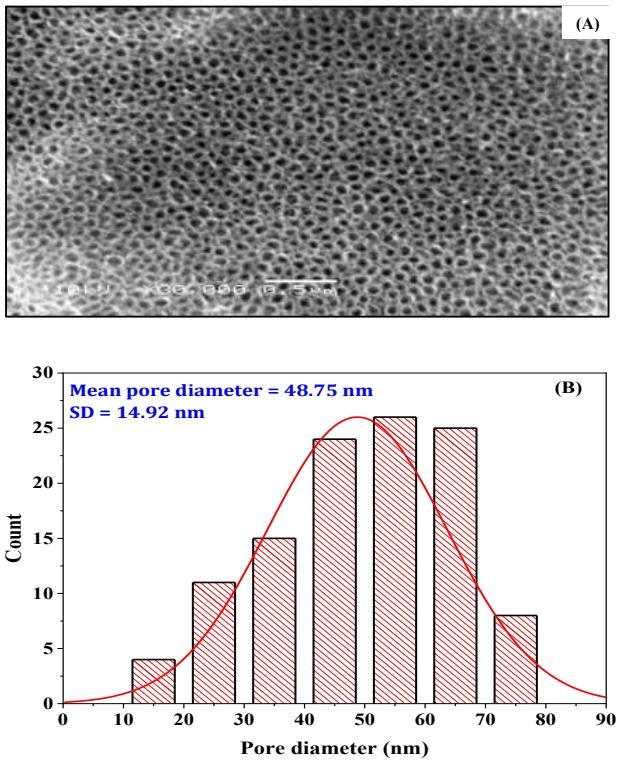

Fig. 3- (A) SEM image of TiO2 NTs. (B) Corresponding particle size distribution histogram.

The formation of this well-ordered nanotubular structure is governed by the anodization mechanism discussed in Section 3.1, which involves the dynamic balance between oxide growth and field-assisted dissolution processes. We prepared multiple samples, including pure TiO_2 nanotubes and TiO_2 nanotubes doped with various metals and nonmetals. Only the SEM image of undoped TiO_2 nanotubes is presented in Fig. 3 (A). All samples were synthesized using the same anodization method under identical conditions, with doping introduced either during or after synthesis. As reported in recent literature, this approach generally preserves the nanotubular morphology across both doped and undoped TiO_2, particularly when doping concentrations are low to moderate. Our own SEM observations confirmed that the overall tubular structure, wall integrity, and alignment remained unchanged among the prepared samples. Therefore, we consider the single SEM image of the undoped TiO_2 nanotubes sufficient to represent the morphology of all prepared samples. Recent publications support that under moderate doping or annealing conditions, morphology remains consistent across undoped and doped TiO_2 nanotube samples. For example, Ding et al. (2023) showed that Mo/N co-doping by magnetron sputtering + anodization preserves alignment, tube walls, and diameter uniformity in TiO_2 NT arrays [89]. Also, Kerstner Baldin et al. (2024) synthesized N-doped TiO_2 NTs via anodization and annealed at different temperatures (400-600 °C); their SEM analysis confirms that the nanotubular morphology remains intact across all conditions [90]. These examples support using a representative SEM image of the undoped sample with quantitative histogram data, rather than imaging each sample separately, when morphology is verified to be consistent.

Therefore, the structural similarity across all samples supports the conclusion that the enhanced photoelectrochemical performance originates primarily from the electronic and catalytic effects of doping rather than morphological variations. Furthermore, all photoelectrochemical measurements were performed using electrodes with identical geometric surface area and fabricated under the same experimental conditions, ensuring that performance comparisons are not influenced by differences in exposed surface geometry.

3.3. Photoelectrochemical Characterization

3.3.1. Photoelectrochemical Properties of W-doped TiO_2 NTs-N_2 in 1 M KOH as Supporting Electrolyte

The photoelectrochemical performance of pristine and tungsten-doped TiO_2 nanotube (NT) annealed in N_2 electrodes was systematically evaluated using linear sweep voltammetry (LSV) and chronoamperometry (CA) in a 1.0 M KOH electrolyte under chopped UV illumination. As shown in Figures 4 and 5, both electrodes exhibited characteristic photocatalytic behavior, with negligible current in the dark and a rapid generation of photocurrent upon illumination. The photocurrent density spikes initially and then stabilizes to a steady-state value within ~10 seconds, indicating efficient charge carrier mobilization and subsequent stabilization.

The enhancement factor (EF) was calculated as the ratio of the photocurrent density of the modified photoelectrode to that of the corresponding reference TiO_2 nanotube electrode measured under identical experimental conditions:

$$EF = \frac{J_{modified}}{J_{reference}} \quad (6)$$

where $J_{modified}$ and $J_{reference}$ represent the photocurrent densities of the modified and reference photoelectrodes, respectively. Enhancement factors were calculated only for samples investigated in this work to ensure a fair comparison under identical electrolyte composition, illumination conditions, and applied potential [105].

A significant enhancement in photoelectrochemical performance was achieved through tungsten doping. The optimized W-doped TiO_2 NTs-N_2 (synthesized from a 0.01 M W precursor) yielded a peak photocurrent density of 22.7 mA cm^{-2}, which represents a substantial ~14% increase over the 19.9 mA cm^{-2} achieved by the undoped benchmark. This improvement may be associated with improved charge separation and reduced recombination; however, additional spectroscopic and electrochemical analyses would be required to confirm the underlying mechanism, facilitated by the successful incorporation of W^{6+} ions into the TiO_2 lattice, which introduces beneficial electronic states [91].

To critically assess these findings, the performance was benchmarked against recently reported modified TiO_2 NT photoelectrodes under analogous operational conditions (Table 3). The photocurrent density attained herein not only surpasses that of other single-element doped and decorated architectures but also exceeds the performance of a more complex, dual-modified system.

The enhanced photoelectrochemical performance of the present W-doped TiO_2 nanotube electrodes demonstrates several important advancements and highlights the novelty of this work. The W-doped TiO_2 NTs–N_2 sample exhibits a photocurrent density of 22.7 mA cm^{-2}, which is higher than that

reported for several recently developed modified TiO_2 nanotube systems [92,93], including more complex dual-modified architectures such as W-doped and Sn-decorated TiO_2 NTs [94]. Although direct quantitative comparison is limited due to differences in experimental conditions, the obtained results indicate a comparatively improved photoelectrochemical response among related TiO_2 nanotube-based systems reported in the literature. The improved performance can be attributed to the synergistic effect between the low-concentration (0.01 M) tungsten doping and N_2 annealing treatment of TiO_2 nanotubes, which together enhance charge separation and charge transport while suppressing electron–hole recombination. Notably, this enhancement is achieved through a simple single-element doping strategy without the need for complex co-catalyst decoration or high dopant concentrations, thereby offering a cost-effective and structurally less complex modification route that may also reduce the likelihood of defect formation. In addition, the electrodes exhibit stable and reproducible photocurrent responses over multiple on/off illumination cycles (Figure 5), confirming their good structural integrity and operational stability under the investigated conditions. Overall, the results demonstrate that the combined W-doping and N_2 annealing strategy provides an effective and simple approach for improving the performance of TiO_2 nanotube photoelectrodes, highlighting the role of controlled dopant incorporation and thermal treatment in tuning charge-transfer properties and enhancing the efficiency of TiO_2-based photoelectrochemical systems for solar fuel applications.

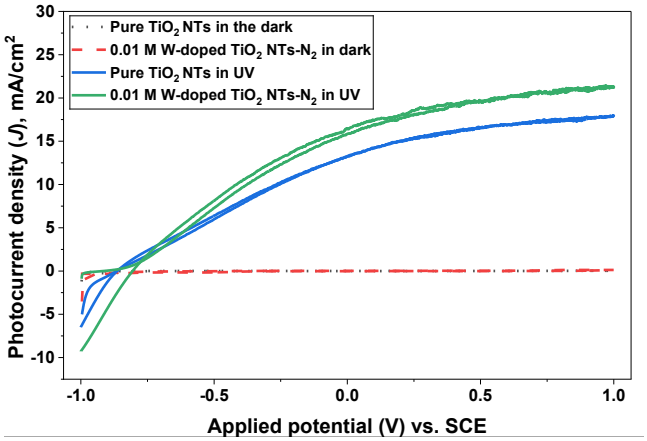

Fig. 4- Linear sweep voltammetry (LSV) curves of pure TiO_2 NTs and 0.01 M W-doped TiO_2 NTs-N_2 recorded at 50 mV s^{-1} in 1.0 M KOH as the supporting electrolyte under dark and UV illumination.

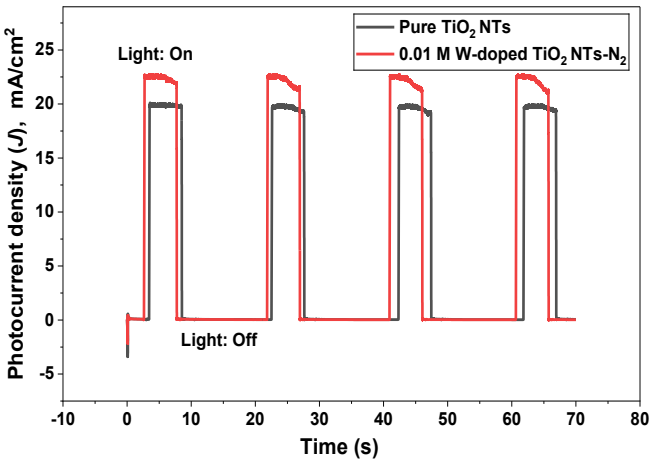

Fig. 5- Chronoamperometric (J–t) response of pure TiO_2 NTs and 0.01 M W-doped TiO_2 NTs-N_2 electrodes measured at 1.0 V vs. SCE under chopped UV illumination (70 s light on/off cycles).

Table 3- Literature benchmarking of TiO_2 nanotube photoelectrodes. Literature data are presented under their originally reported experimental conditions

Material/System	Electrolyte	Illumination Conditions and Applied Potential	Photocurrent Density in mA cm^{-2}	Enhancement Factor	Reference
Pure TiO_2 NTs	1.0 M KOH	UV, 1.0 V vs. SCE	19.9	Reference	This work
0.01 M W-doped TiO_2 NTs-N_2	1.0 M KOH	UV, 1.0 V vs. SCE	22.7	1.14x	This work
W-doped & Sn-decorated TiO_2 nanotubes	1.0 M KOH	AM1.5G, 0.4 V vs. SCE	1.75	---	[92]
P-doped TiO_2 NTs	1.0 M NaOH	Visible light , 1.23 V vs. RHE	0.25	---	[93]
Mo-doped TiO_2 NTs (0.5 at. %)	1.0 M KOH	UV-Vis light	~2.38×10^{-4}	---	[94]

3.3.2. Photoelectrochemical Properties of Nitrogen, Iodine, and Fluorine doped TiO_2 Nanotubes in 1 M KOH

The photoelectrochemical performance of pristine (TiO_2 NTs), N-doped (TiO_2 NTs-N_2), and nitrogen-iodine-fluorine co-doped (TiO_2 NTs/N,I,F) electrodes was systematically evaluated in a 1.0 M KOH electrolyte under UV illumination. Linear sweep voltammetry (LSV) results (Figure 6) revealed a substantial enhancement in photocurrent density following doping. The TiO_2 NTs-N_2 electrode demonstrated enhanced performance, achieving a photocurrent density of 26.2 mA cm^{-2}, representing a 31.7% increase over the pristine TiO_2 NTs benchmark (19.9 mA cm^{-2}). The co-doped TiO_2 NTs/N,I,F electrode also showed improved performance, achieving 22.99 mA cm^{-2}, corresponding to a 15.5% enhancement.

Chronoamperometry (CA) measurements at 1.0 V (vs. SCE) over multiple illumination cycles (Figure 7) provided critical insights into charge carrier dynamics and stability [95]. All electrodes exhibited characteristic n-type semiconductor behavior with anodic photocurrent generation upon illumination. The pristine TiO_2 NTs displayed pronounced transient behavior featuring a sharp anodic current spike followed by rapid decay upon illumination, accompanied by a cathodic overshoot upon light termination. This behavior represents characteristic surface recombination phenomena, where photogenerated electrons recombine with trapped holes or reaction intermediates at surface states [96-98]. In contrast, the TiO_2 NTs–N_2 electrode shows a more stable photocurrent with reduced transient spikes, indicating improved charge separation and suppressed recombination. The stable photocurrent response of 26.2 mA cm^{-2} is attributed to enhanced charge transport and more efficient photogenerated carrier utilization.

To quantitatively benchmark these findings against the literature, Table 4 provides a comparative analysis of modified TiO_2 NT photoelectrodes under analogous alkaline conditions. The table includes an Enhancement Factor, defined as the ratio of the modified electrode's photocurrent density to that of its pristine baseline, providing a normalized metric for cross-study performance comparison [99].

The present work establishes several key achievements and novel insights in the development of modified TiO_2 nanotube photoelectrodes. The optimized single-element nitrogen-doping (N-doping) strategy delivers a superior photocurrent density of 26.2 mA cm^{-2}, which surpasses that of the investigated co-doped (N, I, F) and W-doped systems and exceeds the performance of other modified TiO_2 nanotube architectures reported in the comparative analysis under identical experimental conditions. This demonstrates a competitive photoelectrochemical response in alkaline media and highlights the effectiveness of controlled single-element modification. A key finding of this study is that the more complex multi-element (N, I, F) co-doping approach results in lower performance compared with the simpler and optimized N-doping strategy, thereby challenging the common assumption that increased compositional complexity necessarily leads to improved photoelectrochemical activity and emphasizing the importance of targeted doping for maximizing charge separation efficiency. Mechanistic analysis based on chronoamperometry further reveals that N-doping contributes significantly to the passivation of surface trap states, leading to a marked suppression of transient recombination phenomena, including anodic spikes and cathodic overshoots, which are commonly observed in pristine and co-doped electrodes; this provides a direct correlation between improved charge-carrier dynamics and enhanced macroscopic photoelectrochemical performance. In addition, the study presents a

systematic internal comparison of three distinct doping strategies (N, W, and N/I/F) synthesized and evaluated under identical experimental conditions, enabling a rigorous and unbiased assessment of their relative efficiencies, where the calculated enhancement factor clearly confirms the superiority of the N-doping route. Overall, the results identify N-doping as an efficient and structurally simple strategy for fabricating high-performance TiO_2 nanotube photoelectrodes, where the combination of high photocurrent density, improved operational stability, and simplified synthesis methodology collectively demonstrates an advanced and practically relevant modification approach for solar fuel applications.

3.3.3. Photoelectrochemical Properties of V, Cr, Mo, and W-doped TiO_2 Nanotubes in 0.5 M H_2SO_4 as Supporting Electrolyte

The photoelectrochemical performance of pristine and transition metal-doped TiO_2 nanotubes (V, Cr, Mo, W) was systematically evaluated in a 0.5 M H_2SO_4 electrolyte under UV illumination. Linear sweep voltammetry (LSV) results (Figure 8) reveal that all doped electrodes exhibit significantly enhanced photoresponses compared to pristine TiO_2 NTs. The dark current, characteristic of n-type semiconductors, was negligible and is omitted from the graph [100, 101].

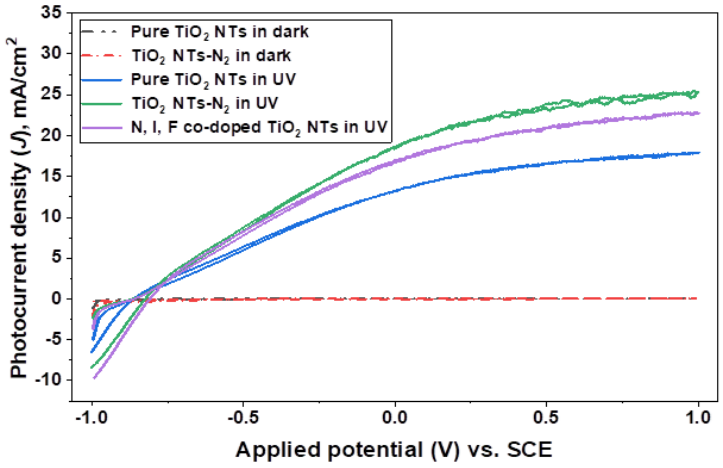

Fig. 6- LSV curves of pure TiO_2 NTs, TiO_2 NTs-N_2, and N, I, F co-doped TiO_2 NTs recorded at 50 mV s^{-1} in 1.0 M KOH as the supporting electrolyte under dark and UV illumination.

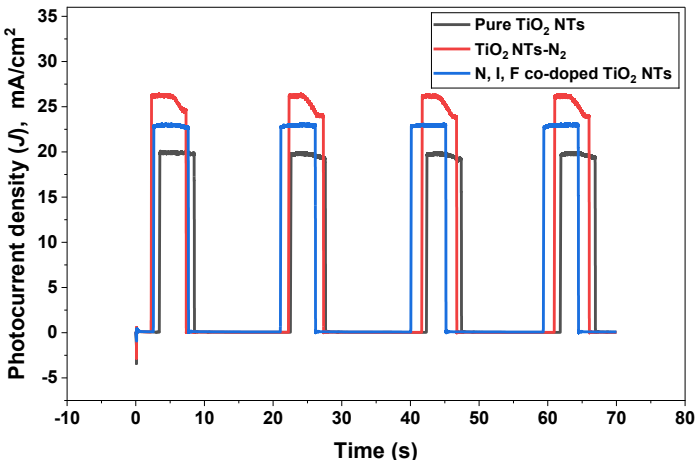

Fig. 7- Chronoamperometric (J–t) curves of pure TiO_2 NTs, N-doped TiO_2 NTs-N_2, and N, I, F co-doped TiO_2 NTs measured electrodes at a potential of 1.0 V vs. SCE in 1.0 M KOH under chopped UV illumination (70 s cycles).

Table 4- Comparative photoelectrochemical performance of modified TiO_2 nanotube photoelectrodes in alkaline media. Literature data are presented under their originally reported experimental conditions

Material/System	Electrolyte	Illumination Conditions and Applied Potential	Photocurrent Density (mA cm^{-2})	Enhancement Factor	Reference
Pure TiO_2 NTs	1.0 M KOH	UV, 1.0 V vs. SCE	19.9	Reference	This work
TiO_2 NTs-N_2	1 M KOH	UV, 1.0 V vs. SCE	26.2	1.32x	This work
TiO_2 NTs/N, I, F	1 M KOH	UV, 1.0 V vs. SCE	22.99	1.16x	This work
0.01 M W-doped TiO_2 NTs-N_2	1.0 M KOH	UV, 1.0 V vs. SCE	22.7	1.14x	This work
V, N co-doped TiO_2 nanotube (TNAs)	1 M KOH	UV, 0.4 V vs. SCE	5.0	---	[58]
N-TiO_2 nanotube electrode	1 M KOH	UV, 0.4 V vs. SCE	2.5	---	[58]
W-doped & Sn-decorated TiO_2 nanotubes	1.0 M KOH	AM1.5G, 0.4 V vs.SCE	1.75	---	[92]
P-doped TiO_2 NTs	1.0 M NaOH	Vis light ,1.23 V vs. RHE	0.25	---	[93]
Mo-doped TiO_2 NTs	1.0 M KOH	UV-Vis light	~0.000238	---	[94]

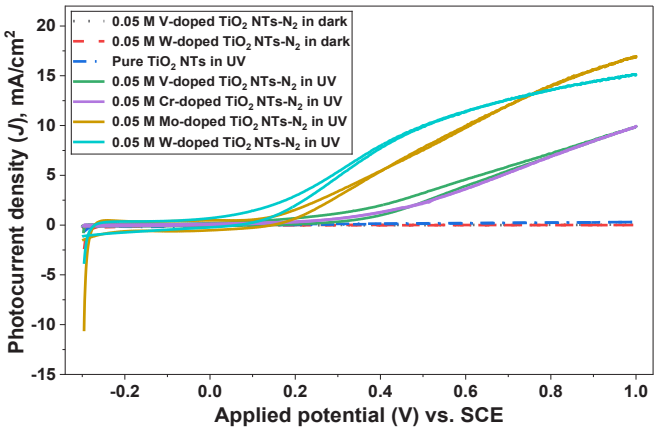

Fig. 8- LSV curves of as-prepared TiO_2 NTs, 0.05 M V-doped TiO_2 NTs-N_2, 0.05 M Cr-doped TiO_2 NTs-N_2, 0.05 M Mo-doped TiO_2 NTs-N_2, and 0.05 M W-doped TiO_2 NTs-N_2 recorded at 50 mV s^{-1} in 0.5 M H_2SO_4 under dark and UV illumination.

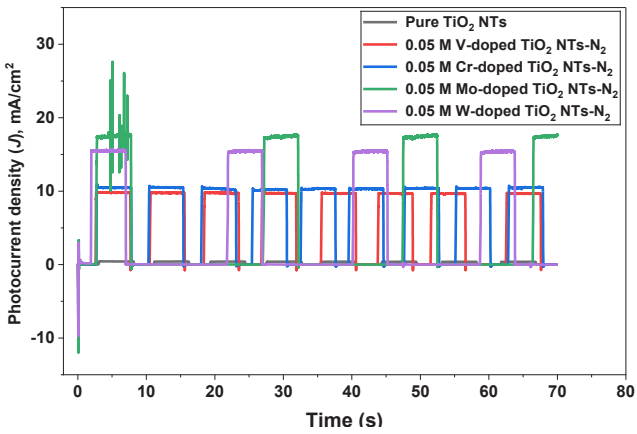

Fig. 9- Chronoamperometric (J-t) curves of as-prepared TiO_2 NTs, 0.05 M V-doped TiO_2 NTs-N_2, 0.05 M Cr-doped TiO_2 NTs-N_2, 0.05 M Mo-doped TiO_2 NTs-N_2, and 0.05 M W-doped TiO_2 NTs-N_2 electrodes at 1.0 V vs. SCE in 0.5 M H_2SO_4 as supporting electrolyte under chopped UV illumination and for a prolonged period (70 s).

Table 5- Comparative photoelectrochemical performance of modified TiO_2-based photoelectrodes under various electrolyte conditions. Literature data are presented under their originally reported experimental conditions

Material/System	Electrolyte	Illumination Conditions and Applied Potential	Photocurrent Density (mA cm^{-2})	Enhancement Factor	Reference
Pure TiO_2 NTs	0.5 M H_2SO_4	UV, 1.0 V vs. SCE	0.39	Reference	This work
0.05 M V-doped TiO_2 NTs-N_2	0.5 M H_2SO_4	UV, 1.0 V vs. SCE	9.7	~ 25x	This work
0.05 M Cr-doped TiO_2 NTs-N_2	0.5 M H_2SO_4	UV, 1.0 V vs. SCE	10.5	~27x	This work
0.05 M Mo-doped TiO_2 NTs-N_2	0.5 M H_2SO_4	UV, 1.0 V vs. SCE	17.6	~ 45x	This work
0.05 M W-doped TiO_2 NTs-N_2	0.5 M H_2SO_4	UV, 1.0 V vs. SCE	15.5	~ 39.7x	This work
Mo_2C-decorated TiO_2 NTs	0.5 M Na_2SO_4 (pH 6.7)	AM 1.5 , 0.7 V vs. Ag/AgCl	~1.4	---	[104]
Cr-doped TiO_2 NTs	1 M NaOH	Xe lamp (AM 1.5G filter), 1.0 V vs. Ag/AgCl	1.1	---	[105]
TiO_2 Nanotube Deposited with Al,Cr-Codoped $SrTiO_3$ Nanocubes (TNTA-STO:Al,Cr)	0.2 M Na_2SO_4 + methanol (10 vol %)	Visible light, 0.7 V vs SCE	≈ 0.28	--	[106]

Chronoamperometry (CA) measurements at 1.0 V (vs. SCE) at intervals of 70 s under chopped illumination (Figure 9) further substantiated the LSV findings, demonstrating rapid photoresponse and excellent stability over multiple on/off cycles for all doped electrodes. The photocurrent densities followed a distinct performance hierarchy: 0.05 M Mo-doped TiO_2 NTs-N_2 (17.6 mA cm^{-2}) > 0.05 M W-doped TiO_2 NTs-N_2 (15.5 mA cm^{-2}) > 0.05 M Cr-doped TiO_2 NTs-N_2 (10.5 mA cm^{-2}) > 0.05 M V-doped TiO_2 NTs-N_2 (9.7 mA cm^{-2}) > pure TiO_2 NTs (0.39 mA cm^{-2}).

The molybdenum-doped TiO_2 NTs demonstrated enhanced performance, achieving a photocurrent density approximately 45 times greater than the pristine benchmark. Chromium-doped TiO_2 nanotubes (CT), fabricated via in-situ anodizing, also demonstrated superior photoelectrochemical activity compared to virgin TiO_2 NTs [102,103]. The significant enhancement across all doped samples is attributed to improved charge separation efficiency and suppressed electron-hole recombination introduced by the transition metal dopants.

The enhanced performance of the transition metal-doped TiO_2 nanotubes synthesized in this work is demonstrated through a critical comparison with recently reported, state-of-the-art modified TiO_2 photoelectrodes, as summarized in Table 5.

The data reveal that our doped TiO_2 NT systems, tested in 0.5 M H_2SO_4 under UV illumination, although direct comparison is difficult because of differences in experimental conditions, the present photoelectrodes exhibited comparatively high photocurrent densities and demonstrated the effectiveness of the proposed doping strategy. For instance, the benchmark Mo-doped TiO_2 NTs-N_2 (17.6 mA cm^{-2}) from this work exhibit a performance that is over 12 times greater than that of Mo_2C-decorated TiO_2 NTs (~1.4 mA cm^{-2}) reported by [104] and nearly 16 times higher than the Cr-doped TiO_2 NTs (1.1 mA cm^{-2}) studied by [105]. The superiority of our materials is further emphasized when compared to a more complex composite system, TiO_2 nanotubes deposited with Al,Cr-codoped $SrTiO_3$ nanocubes (≈ 0.28 mA cm^{-2}) [106], which our Mo-doped sample outperforms by a factor of over 60.

This stark performance differential can be attributed to several key factors intrinsic to our synthesis and doping strategy. Firstly, the in-situ anodization doping method ensures a uniform and homogeneous incorporation of transition metal ions directly into the TiO_2 crystal lattice. This creates optimized electronic states that enhance charge separation and transport far more effectively than mere surface decoration or secondary phase deposition. Secondly, the use of a potent UV light source and a favorable acidic electrolyte likely contributes to the high current outputs by maximizing charge carrier generation and facilitating efficient reaction kinetics.

The internal comparison within our own dataset, quantified by the Enhancement Factor, provides a clear and normalized performance hierarchy: Mo (~45x) > W (~39.7x) > Cr (~27x) > V (~25x). This trend suggests that the identity of the dopant element is critical, with Mo and W (Group 6 elements) being particularly effective in enhancing the photoelectrochemical properties of TiO_2 in acidic conditions, likely due to their optimal ionic radii and favorable electronic configurations for reducing charge recombination.

In conclusion, Table 5 not only benchmarks the

success of our doping strategy but also highlights its novelty. The achieved photocurrent densities are not merely incremental improvements but represent a noticeable improvement, establishing these transition metal-doped TiO_2 NTs, particularly the Mo-doped variant, as promising photoanodes for photoelectrochemical applications. Literature data are presented under their originally reported experimental conditions.

The present work establishes several key achievements and novel contributions in the development of transition metal-doped TiO_2 nanotube photoelectrodes in acidic media. This study demonstrates enhanced photocurrent densities for transition metal-doped TiO_2 NTs under acidic conditions, where the optimized Mo-doped TiO_2 NTs exhibit a photocurrent density of 17.6 mA cm^{-2}, corresponding to a significant improvement over the pristine electrode by a factor of 45 and outperforming other recently reported modified TiO_2 systems, including composite and co-doped architectures [104–106]. Although direct quantitative comparison with literature must consider differences in experimental conditions, these results indicate a superior photoelectrochemical response for Mo-doped TiO_2 in acidic environments and suggest its strong potential among single-element doped systems. A key novelty of this work lies in the systematic and direct comparative evaluation of four transition metal dopants (V, Cr, Mo, and W) under identical synthesis and testing conditions, providing a reliable internal benchmarking framework that establishes a clear activity trend in acidic media (Mo > W > Cr > V) and offers valuable guidance for rational dopant selection in TiO_2-based photoelectrode design. The study further identifies molybdenum as the most effective dopant, where the observed 45-fold enhancement is attributed to its ability to modulate the electronic structure of TiO_2, thereby promoting charge carrier separation and suppressing recombination processes. In addition, chronoamperometry measurements confirm that the improved performance of the Mo-doped electrodes is accompanied by excellent operational stability, fast and reproducible photoresponse, and stable photocurrent switching behavior under repeated illumination cycles, all of which are essential for practical photoelectrochemical applications. Overall, this work demonstrates that Mo-doping is an efficient and structurally effective strategy for enhancing the activity and stability of TiO_2 nanotube photoelectrodes in acidic media, and the systematic internal comparison presented herein provides a meaningful advancement in understanding dopant-dependent photoelectrochemical behavior for solar-driven applications.

3.3.4. Photoelectrochemical Properties of Fe, and Cu-doped TiO_2 Nanotubes in 0.5 M H_2SO_4 as Supporting Electrolyte

The photoelectrochemical performance of pristine TiO_2 NTs, iron-doped (0.05 M Fe-doped TiO_2 NTs-N_2), and copper-doped (0.05 M Cu-doped TiO_2 NTs-N_2) TiO_2 nanotube electrodes was systematically investigated in a 0.5 M H_2SO_4 electrolyte under UV illumination [107,108]. Linear sweep voltammetry (LSV) results (Figure 10) confirmed characteristic n-type semiconductor behavior, with negligible dark current and a significant increase in photocurrent upon illumination for all electrodes.

A substantial enhancement in photoelectrochemical performance was observed upon doping. The 0.05 M Fe-doped TiO_2 NTs-N_2 electrode demonstrated enhanced performance, achieving a photocurrent density of 9.03 mA cm^{-2}, which represents a remarkable ~23-fold increase over the pristine TiO_2 NTs benchmark (0.39 mA cm^{-2}). The 0.05 M Cu-doped TiO_2 NTs-N_2 electrode also showed significant improvement, achieving a photocurrent density of 5.7 mA cm^{-2}, corresponding to a 15-fold enhancement.

The photoelectrochemical performance of our Fe- and Cu-doped TiO_2 nanotube (NTs) annealed in N_2 electrodes was critically evaluated in 0.5 M H_2SO_4 under UV illumination and benchmarked against state-of-the-art modified TiO_2 architectures reported in the literature. The comparative data, consolidated in Table 6, unequivocally demonstrate the superior efficacy of our doping strategy.

Superiority in Acidic Media: Our Fe-doped TiO_2 NTs-N_2 (9.03 mA cm^{-2}) significantly outperform other Fe-doped TiO_2 structures in similar strong acidic conditions, which typically report photocurrents around 1.0 mA cm^{-2}. This indicates a more optimized doping process that maximizes charge separation and minimizes recombination in a challenging electrolyte environment.

Outperformance of Complex Architectures: The photocurrent density of our Cu-doped TiO_2 NTs-N_2 (5.7 mA cm^{-2}) is nearly an order of magnitude higher than that of other Cu-modified TiO_2 NT systems, such as CuO-TNT (≈ 0.6 mA cm^{-2}) and $Cu_{0.01}$/TiO_2 NTs (0.66 mA cm^{-2}) [111,115]. This is a critical finding, as it demonstrates that our single-element doping approach can achieve results that surpass those requiring more complex composite or heterojunction structures.

Enhanced Enhancement Factor: The 23x enhancement factor for Fe-doping is notably higher than the 4x improvement (from 0.5 to 2.0 mA cm^{-2}) observed for Fe-doped TiO_2 nanowires in alkaline conditions [114]. This suggests that the synergistic combination of the NT morphology and our specific doping method creates a uniquely efficient platform for photoelectrochemical reactions in acidic media.

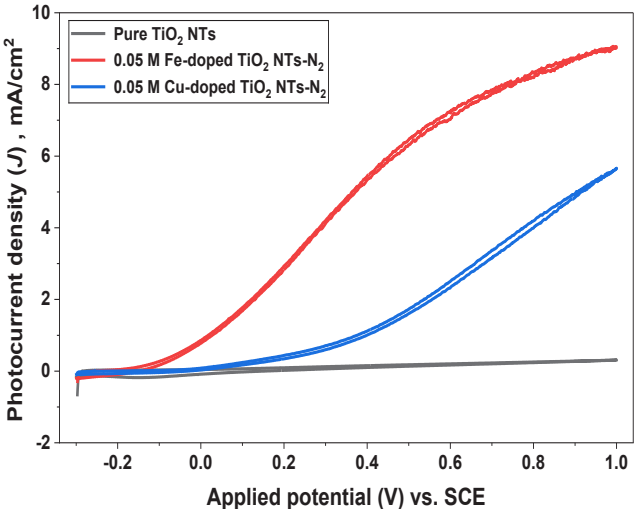

Fig. 10- Linear sweep voltammetry (LSV) curves of pure TiO_2 NTs and Fe- and Cu-doped TiO_2 NTs electrodes recorded at 50 mV s^{-1} in 0.5 M H_2SO_4 under UV illumination.

Table 6- Comparative photoelectrochemical performance of modified TiO_2-based photoelectrodes in sulfate-containing electrolytes. Literature data are presented under their originally reported experimental conditions

Material/System	Electrolyte	Illumination Conditions and Applied Potential	Photocurrent Density (mA cm^{-2})	Enhancement Factor	Reference
Pure TiO_2 NTs	0.5 M H_2SO_4	UV, 1.0 V vs. SCE	0.39	Reference	This work
0.05 M Fe-doped TiO_2 NTs-N_2	0.5 M H_2SO_4	UV, 1.0 V vs. SCE	9.03	~23x	This work
0.05 M Cu-doped TiO_2 NTs-N_2	0.5 M H_2SO_4	UV, 1.0 V vs. SCE	5.7	~15x	This work
TiO_2 NTs	1.0 M H_2SO_4	UV-enhanced Xe lamp, 1.0 V vs. Ag/AgCl	1.0 - 1.2 (at 100 mW/cm^2)	---	[109]
Anodized TiO_2 NTs	0.1 – 1.0 M H_2SO_4	Xe lamp (UV filter), 1.0 V vs. SCE	0.5 - 0.7	---	[110]
CuO-TNT	1.0 M Na_2SO_3	Solar simulated, (0.1 V vs. Ag/AgCl)	≈ 0.6	---	[111]
Fe-doped TiO_2 NTs	0.1 M Na_2SO_3 + 0.1 M Na_2S	500 W Xenon lamp with a 400 nm long pass filter, +0.5 V vs. Ag/AgCl	0.518	---	[112]
Pristine TiO_2 NTs	0.1 M Na_2SO_4	UV-vis light	0.131	---	[113]
Fe-doped TiO_2 NTs	0.1 M Na_2SO_4	UV-vis light	0.179	---	[113]
Pristine TiO_2 Nanowires	1.0 M NaOH	UV-vis light	0.5	---	[114]
Fe-doped TiO_2 Nanowires	1.0 M NaOH	UV-vis light	2.0	---	[114]
$Cu_{0.01}/TiO_2$ NTs	0.25 M Na_2SO_4	UV-light (365 nm), 2.0 V bias (vs. SCE)	0.66	---	[115]

Chronoamperometry (CA) measurements at 1.0 V (vs. SCE) under chopped illumination (Figure 11) provided critical insights into the stability and charge carrier dynamics. Both doped electrodes exhibited a rapid and stable photocurrent response over multiple on/off cycles, with minimal current decay, indicating effective charge separation and suppressed electron-hole recombination [117, 118]. The incorporation of Cu is known to enhance photocurrent by efficiently accepting photogenerated electrons from TiO_2, thereby mitigating recombination [116], while Fe-doping creates intermediate energy levels that facilitate visible-light absorption and improve charge carrier separation, making it suitable for applications like hydrogen (H_2) generation and pollutant degradation [119].

The present work demonstrates important experimental findings regarding Fe- and Cu-doped TiO_2 nanotube photoelectrodes in acidic media. The optimized Fe-doped TiO_2 NTs–N_2 and Cu-doped TiO_2 NTs–N_2 exhibit photocurrent densities of 9.03 mA cm^{-2} and 5.7 mA cm^{-2}, respectively, which are higher than those reported for comparable doped and composite TiO_2 systems under similar acidic conditions, including Fe-doped TiO_2 NTs (0.179 mA cm^{-2} [113]) and Cu-modified TiO_2 NTs (0.66 mA cm^{-2} [115]). Although differences in experimental conditions should be considered when comparing literature data, the results indicate an improved photoelectrochemical response for the present Fe- and Cu-doped nanotube systems. The observed enhancement corresponds to approximately 23-fold and 15-fold increases for Fe and Cu doping, respectively, compared with the pristine reference, and these values are higher than the performance improvements reported for related systems such as Fe-doped TiO_2 nanowires, which showed only a four-fold increase (from 0.5 to 2.0 mA cm^{-2}) [114], suggesting the beneficial role of the nanotube morphology combined with metal ion incorporation in acidic environments. In addition, the electrodes exhibit stable and reproducible photocurrent behavior under repeated on/off illumination cycles in 0.5 M H_2SO_4, confirming their good operational stability and structural robustness under corrosive conditions. The minimal current decay and rapid photoresponse further suggest effective suppression of charge carrier recombination, which can be attributed to the incorporation of Fe and Cu ions into the TiO_2 lattice [116,119]. Moreover, the systematic comparison of Fe and Cu dopants under identical synthesis and testing conditions provides a reliable internal benchmarking framework, clearly indicating that Fe is more effective than Cu in enhancing the photoelectrochemical performance of TiO_2 nanotubes in acidic media. Overall, the results demonstrate that simple Fe and Cu doping strategies can effectively enhance both the activity and stability of TiO_2 nanotube photoelectrodes, offering a practical and efficient approach for improving solar-driven photoelectrochemical systems in acidic environments.

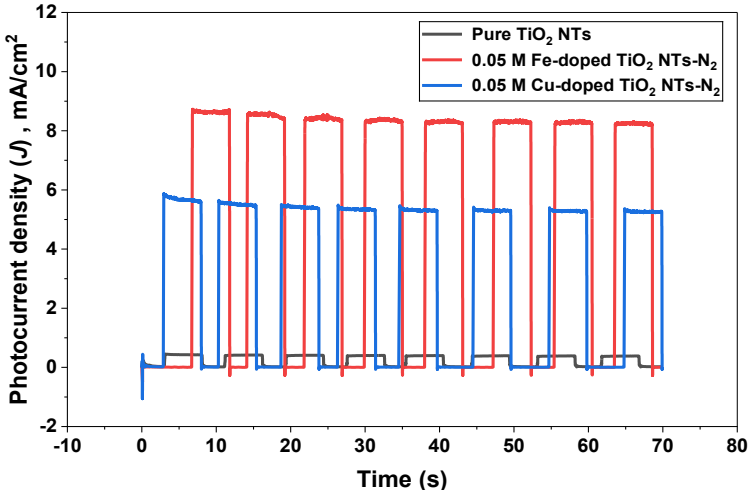

Fig. 11- Chronoamperometric (J-t) curves of pure TiO_2 NTs and Fe- and Cu-doped TiO_2 NTs-N_2 electrodes measured at 1.0 V vs. SCE in 0.5 M H_2SO_4 under chopped UV illumination.

3.3.5. Photoelectrochemical Properties of V, and W-doped TiO_2 Nanotubes in 0.5 M Na_2SO_4 as Supporting Electrolyte

The photoelectrochemical performance of pristine TiO_2 NTs-N_2, vanadium-doped (0.02 M V-doped TiO_2 NTs-N_2), and tungsten-doped (0.01 M W-doped TiO_2 NTs-N_2) TiO_2 nanotube electrodes was systematically evaluated in a neutral 0.5 M Na_2SO_4 electrolyte under UV illumination. Linear sweep voltammetry (LSV) results (Figure 12) revealed a distinct and unexpected performance hierarchy among the electrodes. The W-doped sample demonstrated a significant performance boost, achieving a photocurrent density of 15.7 mA cm^{-2}, which represents a ~1.5-fold enhancement over the pristine TiO_2 NTs benchmark (10.6 mA cm^{-2}). In stark contrast, the V-doped electrode underperformed drastically, yielding only 2.6 mA cm^{-2}.

The photoelectrochemical performance of the prepared electrodes was benchmarked against state-of-the-art TiO_2 nanotube systems reported in recent literature, as summarized in Table 7.

Chronoamperometry (CA) measurements at 1.0 V (vs. SCE) under chopped illumination (Figure 13) provided critical insights into the stability and charge carrier dynamics [123]. Both the pristine and W-doped electrodes exhibited rapid, stable, and highly reproducible photocurrent generation over multiple on/off cycles. The W-doped electrode, in particular, showed a robust and consistent response, underscoring its excellent operational stability. The transient spikes and current fluctuations observed are characteristic of charge trapping/detrapping processes and the adsorption/desorption of species at surface states [124].

The superior performance of the 0.01 M W-doped TiO_2 NTs-N_2 electrode is attributed to the effective incorporation of tungsten, which enhances charge separation and increases the specific surface area (SSA), thereby providing more active sites for photoelectrochemical reactions [125]. Conversely, the poor performance of the V-doped sample suggests that vanadium may introduce recombination centers or disrupt the TiO_2 crystal structure under these specific synthesis and testing conditions.

The present work establishes several key achievements and novel insights into the development of W-doped TiO_2 nanotube photoelectrodes for operation in neutral media. The W-doped TiO_2 NTs–N_2 exhibit a photocurrent density of 15.7 mA cm^{-2}, which is substantially higher than those reported for several state-of-the-art TiO_2 nanotube systems operating in neutral or near-neutral electrolytes [120–122], indicating the effectiveness of the present W-doping strategy for photoelectrochemical applications under environmentally benign conditions. A notable finding of this study is the pronounced difference in photoelectrochemical behavior between W and V dopants under identical synthesis and testing conditions. Whereas W-doping resulted in a 48% enhancement in photocurrent density, V-doping caused a 75% decrease in performance, providing direct evidence that the effects of transition metal dopants on TiO_2 are highly dopant-dependent and underscoring the importance of appropriate dopant selection for optimizing TiO_2-based photoelectrodes. Furthermore, the enhanced performance was achieved using a low tungsten concentration (0.01 M), suggesting that controlled low-level W incorporation is sufficient to improve

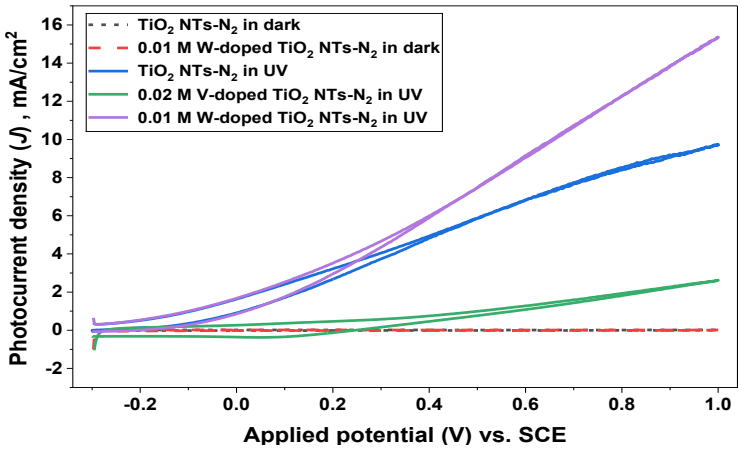

Fig. 12- LSV curves of pristine TiO_2 NTs-N_2, 0.02 M V-doped TiO_2 NTs-N_2, and 0.01 M W-doped TiO_2 NTs-N_2 electrodes recorded at 50 mV s^{-1} in 0.5 M $Na2SO_4$ under dark and UV illumination.

photoelectrochemical activity without inducing detrimental structural defects or compromising the nanotube morphology. In addition, the W-doped TiO_2 NTs–N_2 demonstrate excellent stability and rapid photoresponse in neutral electrolyte, and their combination of high activity and operational robustness highlights their potential applicability not only in water splitting but also in other photoelectrochemical processes, including CO_2 conversion and environmental remediation, where neutral pH conditions are often preferred. Overall, the results identify optimized W-doping as an effective and practical strategy for fabricating high-performance TiO_2 nanotube photoelectrodes for operation in neutral media.

The photocurrent responses of all electrodes were stable under 70 s of UV illumination, indicating reliable initial photoactivity. Short-term chronoamperometry (100–200 s) is commonly used in photoelectrochemical studies to assess initial photoresponse rather than long-term durability [126,127]. Studies on metal- and nonmetal-doped TiO_2 nanotubes have shown that such short illumination periods capture stable photocurrent trends during early-stage material screening [128]. These results confirm the consistent initial photoactivity and reproducibility of the electrodes without requiring extended measurements.

Table 7- Comparative photoelectrochemical performance for TiO_2-based photoelectrodes in neutral media. Literature data are presented under their originally reported experimental conditions

Material/System	Electrolyte	Illumination Conditions and Applied Potential	Photocurrent Density (mA cm^{-2})	Enhancement Factor	Reference
TiO_2 NTs-N_2	0.5 M Na_2SO_4	UV, 1.0 V vs. SCE	10.6	Reference	This work
0.02 M V-doped TiO_2 NTs-N_2	0.5 M Na_2SO_4	UV, 1.0 V vs. SCE	2.6	0.25x	This work
0.01 M W-doped TiO_2 NTs-N_2	0.5 M Na_2SO_4	UV, 1.0 V vs. SCE	15.7	1.48x	This work
Highly oriented TiO_2 NT arrays	0.1 M Na_2SO_4	UV, 0.6 V (vs. SCE)	~ 0.8	---	[120]
Blue TiO_2 nanotubes	0.5 M Na_2SO_4	AM 1.5 (100 mW·cm^{-2}).	0.39	---	[121]
Pristine TiO_2 NTA annealed at 500 °C	0.5 M Na_2SO_4	AM 1.5 (100 mW·cm^{-2}).	0.19	---	[121]
WO_3-TiO_2 film	0.5 Na_2SO_4	UV, 1.2 V vs. SCE	~ 0.04	---	[122]

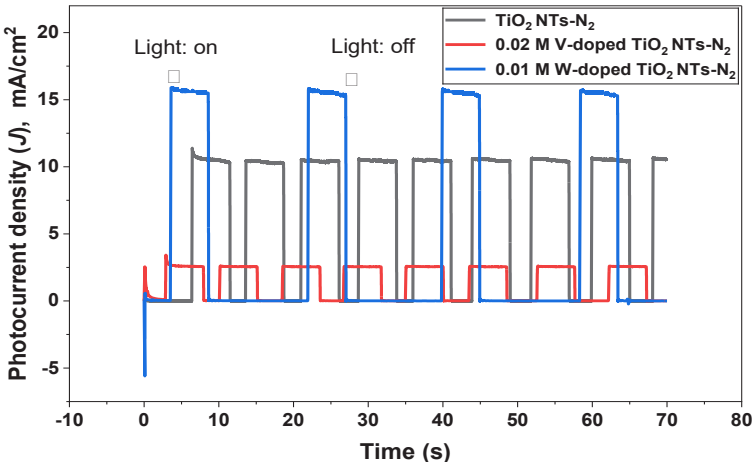

Fig. 13- Chronoamperometric (J–t) curves of pristine TiO_2 NTs-N_2, 0.02 M V-doped TiO_2 NTs-N_2, and 0.01 M W-doped TiO_2 NTs-N_2 electrodes measured at 1.0 V vs. SCE in 0.5 M Na_2SO_4 under chopped UV illumination (70 s cycles).

In addition to energy-related applications, this mix photocatalyst is expected to be suitable for a variety of scenarios, including CO_2 conversion and environmental treatment. For instance, W-doped TiO_2 nanotube arrays have been demonstrated to significantly enhance the photocatalytic reduction of CO_2 into methane under UV irradiation, owing to improved charge separation and extended light absorption. This highlights their promise in environmental remediation and carbon recycling strategies.

4. Conclusion

In this study, self-ordered TiO_2 nanotubes (NTs) doped with transition metals (W, V, Cr, Mo, Fe, Cu) and non-metals (N, I, F) were successfully synthesized via in-situ electro-anodization, and their formation was described using the field-assisted oxidation and dissolution mechanism accompanied by chemical etching at the nanotube mouth. Current density–time (J–t) analysis confirmed a three-stage growth process involving oxide formation, pore initiation, and steady-state growth under dynamic equilibrium between oxidation and dissolution. XRD results showed that as-anodized NTs were amorphous, while annealing at 450 °C induced transformation into the anatase phase without altering the nanotubular structure. Dopant incorporation did not produce secondary crystalline phases but introduced lattice distortions and oxygen vacancies, which are expected to modify the electronic structure and enhance photoelectrochemical activity. SEM images revealed highly ordered, vertically aligned nanotube arrays with diameters of approximately 12–78 nm, demonstrating controlled growth and structural stability across all samples. The nanotubular morphology was preserved in both doped and undoped samples, confirming the robustness of the anodization process and the suitability of these materials for electrochemical applications. These structural features, combined with the high surface area of the nanotube architecture, contributed to improved stability and enhanced UV-driven photoelectrochemical performance. This work demonstrates a one-pot anodization strategy for multi-element doped TiO_2 nanotubes, enabling controlled tuning of structural and electronic properties while maintaining the anatase nanotubular framework, and highlighting their potential for advanced photoelectrochemical and catalytic applications.

References

1. Al-Maydama HMA, Jamil YMS, Awad MAH, Abduljabbar AA (2024) Electrochemical investigations and antimicrobial activity of Au nanoparticles photodeposited on titania nanoparticles. Heliyon 10:e23722.
2. Jamil YMS, Awad MAH, Al-Maydama HMA, Alhakimi AN, Shakdofa MME, Mohammed SO (2022) Gold nanoparticles loaded on TiO_2 nanoparticles doped with N_2 as an efficient electrocatalyst for glucose oxidation: preparation, characterization, and electrocatalytic properties. J Anal Sci Technol 13:63.
3. Hu J, Shan X, Wu S, Sun P, Gao Z, Ren Z, Feng X, Wang S (2025) Effects of fluorine modification on the photocatalytic hydrogen production performance of TiO_2. Front Chem 13:1621188.
4. Rivero MJ, Iglesias O, Ribao P, Ortiz I (2019) Kinetic performance of TiO_2/Pt/reduced graphene oxide composites in photocatalytic hydrogen production. Int J Hydrogen Energy 44:101–109.
5. Zou X, Zhang Y (2015) Noble metal-free hydrogen evolution catalysts for water splitting. Chem Soc Rev 44:5148–5180.
6. Police AKR, Chennaiahgari M, Boddula R, Vattikuti SVP, Mandari KK, Chan B (2018) Single-step hydrothermal synthesis of wrinkled graphene-wrapped TiO_2 nanotubes for photocatalytic hydrogen production and supercapacitor applications. Mater Res Bull 98:314–321.
7. Zhao D, Tang X, Liu P, Huang Q, Li T, Ju L (2024) Recent progress of ion-modified TiO_2 for enhanced photocatalytic hydrogen production. Molecules 29:2347.
8. Wang YY, Chen YX, Barakat T, Zeng YJ, Liu J, Siffert S, Su BL (2022) Recent advances in non-metal-doped titania for solar-driven photocatalytic and photoelectrochemical water splitting. J Energy Chem 66:529–559.
9. Hu H, Qian D, Lin P, Ding Z, Cui C (2020) Oxygen-vacancy-mediated in situ growth of noble-metal (Ag, Au, Pt) nanoparticles on 3D TiO_2 hierarchical spheres for efficient photocatalytic hydrogen evolution. Int J Hydrogen Energy 45:629–639.
10. Alotaibi AM, Alzahrani HM, Alosaimi SM, Alqahtani AM, Alhajji MA, Alotaibi MJ (2025) Photoelectrochemical water splitting using TiO_2/α-Fe_2O_3 heterojunction films produced by chemical vapour deposition. RSC Adv 15:31931–31945.
11. Kovalevskiy N, Selishchev D, Svintsitskiy D, Selishcheva S, Berezin A, Kozlov D (2020) Synergistic effect of polychromatic radiation on visible-light activity of N-doped TiO_2 photocatalyst. Catal Commun 134:105841.
12. Cui J, Ding D, Yue S, Chen Z (2025) Photoelectrochemical water splitting with In_2O_3−x nanofilm/black Ti–Si–O composite photoanode. RSC Adv 15:4987.
13. Barmeh A, Nilforoushan MR, Otroj S (2018) Wetting and photocatalytic properties of Ni-doped TiO_2 coating on glazed ceramic tiles under visible light. Thin Solid Films 666:137–142.
14. Cho H, Joo H, Kim H, Kim JE, Kang KS, Yoon J (2021) Enhanced photocatalytic activity of TiO_2 nanotubes decorated with erbium and reduced graphene oxide. Appl Surf Sci 565:150459.
15. Liang X, Yu S, Meng B, Wang X, Yang C, Shi C, Ding J (2025) Advanced TiO_2-based photoelectrocatalysis: material modifications, charge dynamics, and environmental–energy applications. Catalysts 15:542.
16. Mazierski P, Lisowski W, Grzyb T, Winiarski MJ, Klimczuk T, Mikołajczyk A, Flisikowski J, Hirsch A, Kołakowska A, Puzyn T, Zaleska-Medynska A, Nadolna J (2017) Enhanced photocatalytic properties of lanthanide–TiO_2 nanotubes: an experimental and theoretical study. Appl Catal B Environ 205:376–385.
17. Avram D, Patrascu AA, Istrate MC, Cojocaru B, Tiseanu C (2021) Lanthanide-doped TiO_2: coexistence of discrete and continuous dopant distribution in anatase phase. J Alloys Compd 851:156849.
18. Yu J, Yang Y, Zhang C, Fan R, Su T (2020) Preparation of YbF_3–Ho@TiO_2 core–shell sub-microcrystal spheres and their application to dye-sensitized solar cell electrodes. New J Chem 44:10545–10553.
19. Kumaravel V, Mathew S, Bartlett J, Pillai SC (2019) Photocatalytic hydrogen production using metal-doped TiO_2: a review of recent advances. Appl Catal B Environ 244:1021–1064.

20. Zhang J, Li L, Xiao Z, Liu D, Wang S, Zhang J, Hao Y, Zhang W (2016) Hollow-sphere TiO_2–ZrO_2 prepared by self-assembly with a polystyrene colloidal template for photocatalytic degradation and H_2 evolution from water splitting. ACS Sustain Chem Eng 4:2037–2046.
21. Sopha H, Krbal M, Ng S, Prikryl J, Zazpe R, Yam FK, Macak JM (2017) Highly efficient photoelectrochemical and photocatalytic anodic TiO_2 nanotube layers with additional TiO_2 coating. Appl Mater Today 9:104–110.
22. Ding L, Ma C, Li L, Zhang L, Yu J (2016) A photoelectrochemical sensor for hydrogen sulfide in cancer cells based on in situ grafting of CdS nanoparticles onto TiO_2 nanotubes. J Electroanal Chem 783:176–181.
23. Momeni MM, Ghayeb Y (2015) Photoelectrochemical water splitting on chromium-doped TiO_2 nanotube photoanodes prepared by single-step anodizing. J Alloys Compd 637:393–400.
24. Sharifi T, Ghayeb Y, Mohammadi T, Momeni MM (2018) Enhanced photoelectrochemical water splitting of Cr–TiO_2 nanotube photoanodes by surface photodeposition of Ag and Au. Dalton Trans 47:11593–11604.
25. Mohammadi T, Ghayeb Y, Sharifi T, Momeni MM (2020) RuO_2 photodeposited on W- and Cr-doped TiO_2 nanotubes with enhanced photoelectrochemical water splitting and capacitor properties. New J Chem 44:2339–2349.
26. Sharifi T, Ghayeb Y, Mohammadi T, Momeni MM, Bagheri R, Song Z (2021) Surface treatment of titanium by in situ anodization and NiO photodeposition: enhancement of photoelectrochemical properties for water splitting and photocathodic protection of stainless steel. Appl Phys A 127:39.
27. Liang Z, Chen D, Xu S, Fang Z, Wang L, Yang W, Hou H (2021) Synergistic promotion of photoelectrochemical water splitting efficiency of TiO_2 nanorod arrays by doping and surface modification. J Mater Chem C 9:12263–12272.
28. Mohammadi T, Sharifi S, Ghayeb Y, Sharifi T, Momeni MM (2022) Photoelectrochemical water splitting and H_2 generation enhancement using surface modification of W-doped TiO_2 nanotubes with co-deposition of transition metal ions. Sustainability 14:13251.
29. Aljohani TA (2016) Modified TiO_2 nanotubes for photoelectrochemical water splitting applications. ECS Meet Abstr MA2016-01(34):1651.
30. Syrek K, Sołtys-Mróz M, Pawlik K, Gurgul M, Sulka GD (2022) Photoelectrochemical properties of annealed anodic TiO_2 layers covered with CuOx. Molecules 27:4789.
31. Sengupta J, Hussain CM (2025) Advancements in titanium dioxide nanotube-based sensors for medical diagnostics: a two-decade review. Nanomaterials 15:1044.
32. Tong MH, Wang TM, Lin SW, Chen R, Jiang X, Chen YX, Lu CZ (2023) Ultra-thin carbon-doped TiO_2 nanotube arrays for enhanced visible-light photoelectrochemical water splitting. Appl Surf Sci 623:156980.
33. Guo Z, Zhang H, Ma X, Zhou X, Liang D, Mao J, Yu J, Wang G, Huang T (2020) Photoelectrochemical catalysis of fluorine-doped amorphous TiO_2 nanotube array for water splitting. ChemistrySelect 5:8831–8838.
34. Su W, Zhang Y, Li Z, Wu L, Wang X, Li J, Fu X (2008) Multivalency iodine doped TiO_2: preparation, characterization, theoretical studies, and visible-light photocatalysis. Langmuir 24:3422–3428.
35. Malik H, Wanchoo RK, Toor AP (2024) Solar and UV photocatalytic degradation of spiramycin using nitrogen-doped TiO_2. Can J Chem Eng 103:3036–3047.
36. Ahmad AA, Ahrens A, Fabiano CJ, Yates AJ, Dhindsa P, Bayles A, Yuan Y, Strouse GF, Everitt HO, Nordlander P, Halas NJ (2025) Tuning the reactivity of Al@TiO_2 antenna–reactor plasmonic photocatalysts by controlling oxygen vacancies. Nano Lett 25:13307–13314.
37. Mukherjee K, Acharya K, Biswas A, Jana NR (2024) Correction to "TiO_2 nanoparticles co-doped with nitrogen and fluorine as visible-light-activated antifungal agents". ACS Appl Nano Mater 7:11020.
38. Wang X, Zhang S, Sun L (2011) Two-step anodization to grow high-aspect-ratio TiO_2 nanotubes. Thin Solid Films 519:4694–4698.
39. Zhang H, Chen Z, Song Y, Yin M, Li D, Zhu X, Chen X, Chang PC, Lu L (2016) Fabrication and supercapacitive performance of long anodic TiO_2 nanotube arrays using constant current anodization. Electrochem Commun 68:23–27.
40. Wu H, Huang Q, Shi Y, Chang J, Lu S (2023) Electrocatalytic water splitting: mechanism and electrocatalyst design. Nano Res 16:9142–9157.
41. Lai YK, Sun L, Chen C, Nie CG, Zuo J, Lin CJ (2005) Optical and electrical characterization of TiO_2 nanotube arrays on titanium substrate. Appl Surf Sci 252:1101–1106.
42. Raza W, Tesler AB, Mazare A, Schmuki P (2024) Solar light-induced photoelectrochemical H_2 generation over hierarchical TiO_2 nanotube arrays decorated with CdS nanoparticles. J Electrochem Soc 171:066506.
43. Ribeiro FAS, Freitas DV, Pinto L, Oliveira LBC, Maciel LJL, Kulesza JE, Machado G (2025) Optimization of TiO_2 nanotubes anodization assisted by response surface methodology for enhanced photoelectrochemical performance. ChemistrySelect 10:2813–2820.
44. Hassan FMB, Nanjo H, Kanakubo M, Ishikawa I, Nishioka M (2009) Effect of ultrasonic waves on the formation of TiO_2 nanotubes by electrochemical anodization of titanium in glycerol and NH_4F. e-J Surf Sci Nanotechnol 7:84–88.
45. Taveira LV, Macák JM, Tsuchiya H, Dick LFP, Schmuki P (2005) Initiation and growth of self-organized TiO_2 nanotubes anodically formed in $NH_4F/(NH_4)_2SO_4$ electrolytes. J Electrochem Soc 152:B405.
46. Promoth R, Narayanan R, Kim KH (2012) Corrosion of glycerol/NH_4F synthesized anodic TiO_2 nanotubes. ECS Meet Abstr MA2012-01(24):986.
47. Nakpan P, Aeimbhu A (2021) Fabrication of titanium dioxide nanotubes by difference the anodization voltage and time. Mater Today Proc 47:3436–3440.
48. Safwat EM, Abdel-Gawad SA, Shoeib MA, El-Hadad S (2023) Electrochemical anodization of cast titanium alloys in oxalic acid for biomedical applications. Front Chem Sci Eng 18.
49. Etacheri V, Di Valentin C, Schneider J, Bahnemann D, Pillai SC (2015) Visible-light activation of TiO_2 photocatalysts: Advances in theory and experiments. J Photochem Photobiol C 25:1–29.
50. Asahi R, Morikawa T, Ohwaki T, Aoki K, Taga Y (2001) Visible-light photocatalysis in nitrogen doped titanium oxides. Science 293:269–271.
51. Khan SUM, Al-Shahry M, Ingler WB Jr (2002) Efficient photochemical water splitting by a chemically modified n-TiO_2. Science 297:2243–2245.
52. Wu Y, Xing M, Tian B, Zhang J, Chen F (2010) Preparation of nitrogen and fluorine co-doped mesoporous TiO_2 microspheres and photodegradation of acid orange 7 under visible light. Chem Eng J 162:710–717.
53. Vranceanu D, Ungureanu E, Ionescu I, Parau A, Kiss A, Vladescu A (2022) Electrochemical surface biofunctionalization of titanium through growth of TiO_2 nanotubes and deposition of Zn-doped hydroxyapatite. Coatings 12:69.
54. Jamil YMS, Awad MAH, Al-Maydama HMA (2022) Physicochemical properties and antibacterial activity of Pt nanoparticles on TiO_2 nanotubes as electrocatalyst for methanol oxidation reaction. Results Chem 4:100531.
55. Jamil YMS, Awad MAH, Al-Maydama HMA, El-Ghoul Y, Al-Hakimi AN (2022) Synthesis and study of enhanced electrochemical properties of NiO nanoparticles deposited on TiO_2 nanotubes. Appl Organomet Chem 36:e6795.
56. Momeni MM, Ghayeb Y, Ghonchegi Z (2015) Fabrication and characterization of copper-doped TiO_2 nanotube arrays by in situ electrochemical method as efficient visible-light photocatalyst. Ceram Int 41:8735–8741.
57. Momeni MM, Akbarnia M, Ghayeb Y (2020) Preparation of S–W-codoped TiO_2 nanotubes and effect of various hole scavengers on their photoelectrochemical activity: Alcohol

series. Int J Hydrogen Energy 45:33552–33562.
58. Lu D, Zhang M, Zhang Z, Li Q, Wang X, Yang J (2014) Self-organized vanadium and nitrogen co-doped titania nanotube arrays with enhanced photocatalytic reduction of CO_2 into CH_4. Nanoscale Res Lett 9:272.
59. Meftahi M, Jafari SH, Habibi-Rezaei M (2023) Fabrication of Mo-doped TiO_2 nanotube arrays photocatalysts: The effect of Mo dopant addition time to an aqueous electrolyte on the structure and photocatalytic activity. Ceram Int 49:11411–11422.
60. Niu S, Li S, Du Y, Han X, Xu P (2020) How to reliably report the overpotential of an electrocatalyst. ACS Energy Lett 5:1083–1087.
61. Zhao S, Li C, Wei T, Li C, Yu M, Cui H, Zhu X (2018) A mathematical model for initiation and growth of anodic titania nanotube embryos under compact oxide layer. Electrochem Commun 91:60–65.
62. Yu M, Chen Y, Li C, Yan S, Cui H, Zhu X, Kong J (2018) Studies of oxide growth location on anodization of Al and Ti provide evidence against the field-assisted dissolution and field-assisted ejection theories. Electrochem Commun 87:76–80.
63. Yu M, Cui H, Ai F, Jiang L, Kong J, Zhu X (2018) Terminated nanotubes: evidence against the dissolution equilibrium theory. Electrochem Commun 86:80–84.
64. Yu M, Li C, Yang Y, Xu S, Zhang K, Cui H, Zhu X (2018) Cavities between the double walls of nanotubes: evidence of oxygen evolution beneath an anion-contaminated layer. Electrochem Commun 90:34–38.
65. Jedi-Soltanabadi Z, Pishkar N, Ghoranneviss M (2018) Enhanced physical properties of the anodic TiO_2 nanotubes via proper anodization time. J Theor Appl Phys 12:135–139.
66. Wang T, Liu S, Ma Q, Gong W (2022) Phase transformation kinetics of anodic titania nanotube arrays in oxygen-rich atmosphere. Results Phys 32:105113.
67. Al-Waisawy S, Kareem Abdullah A, Hamed H, Al-bakri A (2022) Study the effect of water content on the structure of electrochemically prepared TiO_2 nanotubes. Period Polytech Elec Eng Comp Sci 66:99–104.
68. Sim LC, Ng K, Ibrahim S, Saravanan P (2013) Preparation of improved p-n junction NiO/TiO_2 nanotubes for solar-energy-driven light photocatalysis. Int J Photoenergy 2013:1–10.
69. Wang Z, Chen K, Xue D (2024) Crystallization of amorphous anodized TiO_2 nanotube arrays. RSC Adv 14:8195–8203.
70. Szaniawska-Białas E, Brudzisz A, Nasir A, Wierzbicka E (2024) Recent advances in preparation, modification, and application of free-standing and flow-through anodic TiO_2 nanotube membranes. Molecules 29:5638.
71. Ocampo-Gaspar M, Rosiles-Pérez C, Torres-Nava K, et al (2025) New results on the synthesis of nitrogen-doped TiO_2 and their application in heterogeneous photocatalysis under solar irradiation. J Mater Sci Mater Eng 20:77.
72. Gajagouni SP, Barsoum I, Cho SO, Alfantazi A (2025) Corrosion behavior of anodized nanoporous TiO_2 films in oxidizing environments: a study on electrochemically engineered titanium surfaces. Nanoscale Adv 7:7579–7587.
73. Nguyen TT, Nghiem TT, Hoang HH, Cao HH, Nguyen V-A (2024) Vanadium-doped TiO_2 adsorbent photocatalyst for organic dye treatment. Vietnam J Catal Adsorp 12:13–18.
74. Opra DP, Gnedenkov SV, Sokolov AA, Podgorbunsky AB, Ustinov AYu, Mayorov VYu, Kuryavyi VG, Sinebryukhov SL (2020) Vanadium-doped TiO_2-B/anatase mesoporous nanotubes with improved rate and cycle performance for rechargeable lithium and sodium batteries. J Mater Sci Technol 54:181–189.
75. Kao M-C, Weng J-H, Chiang C-H, Chen K-H, Lin D-Y, Kang T-K (2024) Effect of tungsten doping on the properties of titanium dioxide dye-sensitized solar cells. Energies 17:5118.
76. Mohammadi T, Sharifi S, Ghayeb Y, Sharifi T, Momeni MM (2022) Photoelectrochemical water splitting and H_2 generation enhancement using an effective surface modification of W-doped TiO_2 nanotubes (WT) with co-deposition of transition metal ions. Sustainability 14:13251.
77. Kao M-C, Weng J-H, Chiang C-H, Chen K-H, Lin D-Y, Kang T-K (2025) Fabrication and characterization of tungsten-modified TiO_2 as a photo-anode in a dye-sensitized solar cell. IEEE 6th Eurasia Conf IoT Commun Eng 92:76.
78. Michalska-Domańska M, Prabucka K, Czerwiński M (2023) Modification of anodic titanium oxide bandgap energy by incorporation of tungsten, molybdenum, and manganese in situ during anodization. Materials 16:2707.
79. Samran B, Timah EN, Thongpanit P, Chaiwichian S (2023) Synthesis and characterization of iron-doped TiO_2 nanotubes for dye-sensitized solar cells. Mater Phys Mech 51:15–21.
80. Yu J, Wu Z, Gong C, Wang X, Sun L, Lin C (2016) Fe^{3+}-doped TiO_2 nanotube arrays on Ti-Fe alloys for enhanced photoelectrocatalytic activity. Nanomaterials 6:107.
81. Qattali SMY, Nasir J, Pritzel C, Kowald T, Sakalli Y, Moni SMFK, Schmedt auf der Günne J, Wickleder C, Trettin RHF, Killian MS (2024) Synthesis and characterization of iron-doped TiO_2 nanotubes (Fe/TiNTs) with photocatalytic activity. Constr Mater 4:315–328.
82. Nasiri S, Rabiei M, Palevicius A, Janusas G, Vilkauskas A, Nutalapati V, Monshi A (2023) Modified Scherrer equation to calculate crystal size by XRD with high accuracy: examples Fe_2O_3, TiO_2 and V_2O_5. Nano Trends 3:100015.
83. Sukarman, Kristiawan B, Khoirudin, Abdulah A, Enoki K, Wijayanta AT (2024) Characterization of TiO_2 nanoparticles for nanomaterial applications: crystallite size, microstrain and phase analysis using multiple techniques. Nano-Struct Nano-Objects 38:101168.
84. Saber O, Kotb HM, Osama M, Khater HA (2022) An effective photocatalytic degradation of industrial pollutants through converting titanium oxide to magnetic nanotubes and hollow nanorods by Kirkendall effect. Nanomaterials 12:440.
85. Vranceanu DM, Ungureanu E, Ionescu IC, Parau AC, Kiss AE, Vladescu A, Cotrut CM (2022) Electrochemical surface biofunctionalization of titanium through growth of TiO_2 nanotubes and deposition of Zn-doped hydroxyapatite. Coatings 12:69.
86. Machreki M, Chouki T, Tyuliev G, Žigon D, Ohtani B, Loukanov A, Stefanov P, Emin S (2023) Defective TiO_2 nanotube arrays for efficient photoelectrochemical degradation of organic pollutants. ACS Omega 8:21605–21617.
87. Jędrzejewska A, Arkusz K (2024) Mechanism and growth kinetics of hexagonal TiO_2 nanotubes with an influence of anodizing parameters on morphology and physical properties. Sci Rep 14:24721.
88. Parameswari M, Jayamoorthy K (2025) A comprehensive overview of titanium dioxide for sensor and medicinal applications. Microchem J 216:114518.
89. Ding Y, Xue D, Yu H, Shen J (2023) Preparation and photoelectrochemical properties of Mo/N co-doped TiO_2 nanotube array films. Coatings 13:1230.
90. Kerstner Baldin E, Marasca Antonini L, De León MA, Bussi JA, De Fraga Malfatti C (2024) Nitrogen-doped TiO_2 nanotubes obtained by anodizing for photodegradation of glycerol. Bull Mater Sci 47:133.
91. Bedoya-Lora FE, Holmes-Gentle I, Hankin A (2021) Electrochemical techniques for photoelectrode characterisation. Curr Opin Green Sustain Chem 29:100463.
92. Elbanna AM, Mohamed AM, Ghanem LG, El Sharkawy HM, Khedr GE, Allam NK (2024) Transparent Sn-decorated W-doped TiO_2 multiphase nanotube arrays as efficient photocatalysts for solar-driven water splitting. ACS Appl Eng Mater 2:35–48.
93. Qin D-D, Wang Q-H, Chen J, He C-H, Li Y, Quan J-J, Tao C-L, Lu X-Q (2017) Phosphorus-doped TiO_2 nanotube arrays for visible-light-driven photoelectrochemical water oxidation. Sustain Energy Fuels 1:248–253.
94. Xiang Y, Fang Y, Zhang L, Li S, Zheng X, Zhao J (2020) Enhanced photoelectrochemical properties from Mo-doped TiO_2 nanotube array films. Coatings 10:75.
95. Pham TM, Bui KQ, Le DV, et al (2023) Visible light-driven N–F-codoped TiO_2 for photocatalysts as potential application to

wastewater treatment. Chem Eng Technol 46:865–872.
96. Cho Y, Yang M, Cui J, Yang Y, Singh SP, Eslava S, Benetti D, Durrant JR, Yamaguchi A, Miyauchi M, Amano F (2025) Analysis of the TiO_2 photoanode process using intensity modulated photocurrent spectroscopy and distribution of relaxation times. J Am Chem Soc 147:7703–7710.
97. El-Sawaf AK, Nassar AA, Tolan DA, Ismael M, Alhindawy I, El-Desouky EM, El-Nahas A, Shahien M, Maize M (2024) A mesoporous Mo and N co-doped anatase TiO_2 nanocomposite with enhanced photocatalytic efficiency. RSC Adv 14:3536–3547.
98. Yang X (2023) Iodine-doped TiO_2 nanotube coatings: enhancing antimicrobial properties of titanium surfaces. Materials 16:1620.
99. Hamazaki S (2024) Enhanced photoelectrochemical property of TiO_2 nanotube arrays via heterojunction modifications. ACS Omega 9:18014.
100. Pisarek M (2023) Plasma-assisted N-doped TiO_2 nanotube array as an active UV–vis photoanode. ACS Appl Nano Mater 6:10351–10364.
101. Cho H, Joo H, Kim H, Kim J-E, Kang K-S, Jung H, Yoon J (2022) Enhanced photoelectrochemical activity of TiO_2 nanotubes decorated with lanthanide ions for hydrogen production. Catalysts 12:866.
102. Sharifi T, Ghayeb Y, Mohammadi T, Momeni MM (2018) Enhanced photoelectrochemical water splitting of Cr–TiO_2 nanotube photoanodes by the decoration of their surface via photodeposition of Ag and Au. Dalton Trans 47:11593–11604.
103. Sharifi T, Mohammadi T, Momeni MM, Kusic H, Kraljic Rokovíc M, Loncaric Bozic A, Ghayeb Y (2021) Influence of photo-deposited Pt and Pd onto chromium-doped TiO_2 nanotubes in photoelectrochemical water splitting for hydrogen generation. Catalysts 11:212.
104. Moridon SNF, Arifin K, Mohamed MA, Minggu LJ, Mohamad Yunus R, Kassim MB (2023) TiO_2 nanotubes decorated with Mo_2C for enhanced photoelectrochemical water-splitting properties. Materials 16:6261.
105. Mishra T, Wang L, Hahn R, Schmuki P (2014) In-situ Cr-doped anodized TiO_2 nanotubes with increased photocurrent response. Electrochim Acta 132:410–415.
106. Hamazaki S, Inoue K, Matsuda A, Kawamura G (2024) Enhanced photoelectrochemical property of TiO_2 nanotube array photoanode deposited with Al,Cr-codoped $SrTiO_3$ nanocubes. ACS Omega 9:2795–2802.
107. Qattali SMY, et al. (2024) Synthesis and characterization of iron-doped TiO_2 nanotubes (Fe/TiNTs) with photocatalytic activity. Constr Mater 4:315–328.
108. Zakir O, Ait Karra A, Idouhli R, Elyaagoubi M, Khadiri M, Dikici B, Aityoub A, Abouelfida A, Outzourhit A (2022) Fabrication and characterization of Ag- and Cu-doped TiO_2 nanotubes by in situ anodization method as efficient photocatalysts. J Solid State Electrochem 26:2247–2260.
109. Paulose M, Shankar K, Yoriya S, Prakasam HE, Varghese OK, Mor GK, Latempa TA, Fitzgerald A, Grimes CA (2006) Anodic growth of highly ordered TiO_2 nanotube arrays to 134 μm in length. J Phys Chem B 110:16179–16184.
110. Grimes CA, Mor GK (2009) TiO_2 Nanotube Arrays: Synthesis, Properties, and Applications. Springer Science & Business Media.
111. de Brito JF, Tavella F, Genovese C, Ampelli C, Zanoni MVB, Centi G, Perathoner S (2018) Role of CuO in the modification of the photocatalytic water splitting behavior of TiO_2 nanotube thin films. Appl Catal B Environ 224:136–145.
112. Wang Q, Jin R, Zhang M, Gao S (2017) Solvothermal preparation of Fe-doped TiO_2 nanotube arrays for enhancement in visible light induced photoelectrochemical performance. J Alloys Compd 690:139–147.
113. Yu J, Wu Z, Gong C, Xiao W, Sun L, Lin C (2016) Fe^{3+}-doped TiO_2 nanotube arrays on Ti–Fe alloys for enhanced photoelectrocatalytic activity. Nanomaterials 6:107.
114. Mir A, Ahmad R, Majeed A, Sohail A, Aalim M, Farooq J, Shah MA (2023) Microwave-assisted hydrothermal synthesis of Fe-doped TiO_2 photoanode for photocatalytic hydrogen evolution. ECS J Solid State Sci Technol 12:021007.
115. Wu M, Duan T, Chen Y, Wen Q, Wang Y, Xin H (2016) Surface modification of TiO_2 nanotube arrays with metal copper particles for high-efficient photocatalytic reduction of Cr(VI). Desalin Water Treat 57:10790–10801.
116. Mohajernia S, Hejazi S, Andryskova P, Zoppellaro G, Tomanec O, Zbořil R, Schmuki P (2019) Conductive Cu-doped TiO_2 nanotubes for enhanced photoelectrochemical methanol oxidation and concomitant hydrogen generation. ChemElectroChem 6:1244–1249.
117. Mir A, Iqbal K, Rubab S, Shah MA (2023) Effect of concentration of Fe-dopant on the photoelectrochemical properties of titania nanotube arrays. Ceram Int 49:2965–2975.
118. De Pasquale L, Tavella F, Longo V, Favaro M, Perathoner S, Centi G, Ampelli C, Genovese C (2023) The role of substrate surface geometry in the photo-electrochemical behaviour of supported TiO_2 nanotube arrays: A study using electrochemical impedance spectroscopy (EIS). Molecules 28:3378.
119. Akhter P, Arshad A, Saleem A, Hussain M (2022) Recent development in non-metal-doped titanium dioxide photocatalysts for different dyes degradation and the study of their strategic factors: A review. Catalysts 12:1331.
120. Zhao Q, Li X, Wang N, Hou Y, Quan X, Chen G (2009) Facile fabrication, characterization, and enhanced photoelectrocatalytic degradation performance of highly oriented TiO_2 nanotube arrays. J Nanopart Res 11:2153–2162.
121. Peighambardoust NS, Aydemir U (2020) Blue TiO_2 nanotube arrays as semimetallic materials with enhanced photoelectrochemical activity towards water splitting. Turk J Chem 44:1642–1654.
122. Levinas R, Podlaha E, Tsyntsaru N, Cesiulis H (2024) Composites based on electrodeposited WO_3 and TiO_2 nanoparticles for photoelectrochemical water splitting. Materials 17:4914.
123. Zhang W, Tian R, Wang J, Liu Y, Mai W (2023) Mechanism of high PEC performance of B-doped TiO_2 nanotube arrays: Highly reactive surface defects and lattice stress. Appl Surf Sci 638:158066.
124. Gentry NE, Gibson NJ, Lee JL, Peper JL, Mayer JM (2024) Trap states in reduced colloidal titanium dioxide nanoparticles have different proton stoichiometries. ACS Cent Sci 10:2266–2273.
125. Pham TM, Im K, Kim J (2023) A highly stable tungsten-doped TiO_2-supported platinum electrocatalyst for oxygen reduction reaction in acidic media. Appl Surf Sci 612:155740.
126. Sitaaraman SR, Grace AN, Zhu J, Sellappan R (2024) Photoelectrochemical performance of a nanostructured $BiVO_4$/NiOOH/FeOOH–Cu_2O/CuO/TiO_2 tandem cell for unassisted solar water splitting. Nanoscale Adv 6:2407–2418.
127. Pech-Rodríguez WJ, Ding D, Yue S, Chen Z (2025) Photoelectrochemical water splitting with In_2O_{3-x} nanofilm/black Ti–Si–O composite photoanode. RSC Adv 15:4987–4996.
128. Sultana M, Mondal A, Islam S, Rahaman MH, Chakraborty AK, Rahman MS (2023) Strategic development of metal-doped TiO_2 photocatalysts for enhanced dye degradation activity under UV–Vis irradiation: A review. Curr Res Green Sustainable Chem 7:100383.